



universe

IMPACT
FACTOR
2.5

CITESCORE
4.3

Article

Constraining the Initial Mass Function via Stellar Transients

Francesco Gabrielli, Lumen Boco, Giancarlo Ghirlanda, Om Sharan Salafia, Ruben Salvaterra, Mario Spera and Andrea Lapi

Special Issue

[Universe: Feature Papers 2024 – Compact Objects](#)

Edited by

Prof. Dr. Nicolas Chamel



<https://doi.org/10.3390/universe10100383>

Article

Constraining the Initial Mass Function via Stellar Transients

Francesco Gabrielli ^{1,2,*}, Lumen Boco ^{1,2,3}, Giancarlo Ghirlanda ^{4,5}, Om Sharan Salafia ^{4,5}, Ruben Salvaterra ⁶, Mario Spera ^{1,2,7} and Andrea Lapi ^{1,2,3,8}

¹ Physics Area, Scuola Internazionale Superiore Studi Avanzati (SISSA), Via Bonomea 265, 34136 Trieste, Italy; lboco@sissa.it (L.B.); mspera@sissa.it (M.S.); lapi@sissa.it (A.L.)

² Istituto Nazionale di Fisica Nucleare (INFN)—Sezione di Trieste, Via Valerio 2, 34127 Trieste, Italy

³ Institute for Fundamental Physics of the Universe (IFPU), Via Beirut 2, 34014 Trieste, Italy

⁴ Osservatorio Astronomico di Brera, Istituto Nazionale di Astrofisica (INAF), Via E Bianchi 46, 23807 Merate, Italy; giancarlo.ghirlanda@inaf.it (G.G.); om.salafia@inaf.it (O.S.S.)

⁵ Istituto Nazionale di Fisica Nucleare (INFN)—Sezione di Milano-Bicocca, Piazza della Scienza 3, 20126 Milano, Italy

⁶ Istituto di Astrofisica Spaziale e Fisica Cosmica di Milano, Istituto Nazionale di Astrofisica (INAF), Via A. Corti 12, 20133 Milano, Italy; ruben.salvaterra@inaf.it

⁷ Osservatorio Astronomico di Roma, Istituto Nazionale di Astrofisica (INAF), Via Frascati 33, 00040 Monteporzio Catone, Italy

⁸ Istituto di Radioastronomia (IRA), Istituto Nazionale di Astrofisica (INAF), Via Gobetti 101, 40129 Bologna, Italy

* Correspondence: fgabriel@sissa.it

Abstract: The stellar initial mass function (IMF) represents a fundamental quantity in astrophysics and cosmology describing the mass distribution of stars from low mass all the way up to massive and very massive stars. It is intimately linked to a wide variety of topics, including stellar and binary evolution, galaxy evolution, chemical enrichment, and cosmological reionization. Nonetheless, the IMF still remains highly uncertain. In this work, we aim to determine the IMF with a novel approach based on the observed rates of transients of stellar origin. We parametrize the IMF with a simple but flexible Larson shape, and insert it into a parametric model for the cosmic UV luminosity density, local stellar mass density, type Ia supernova (SN Ia), core-collapse supernova (CCSN), and long gamma-ray burst (LGRB) rates as a function of redshift. We constrain our free parameters by matching the model predictions to a set of empirical determinations for the corresponding quantities via a Bayesian Markov Chain Monte Carlo method. Remarkably, we are able to provide an independent IMF determination with a characteristic mass $m_c = 0.10_{-0.08}^{+0.24} M_{\odot}$ and high-mass slope $\xi = -2.53_{-0.27}^{+0.24}$ that are in accordance with the widely used IMF parameterizations (e.g., Salpeter, Kroupa, Chabrier). Moreover, the adoption of an up-to-date recipe for the cosmic metallicity evolution allows us to constrain the maximum metallicity of LGRB progenitors to $Z_{max} = 0.12_{-0.05}^{+0.29} Z_{\odot}$. We also find which progenitor fraction actually leads to SN Ia or LGRB emission (e.g., due to binary interaction or jet-launching conditions), put constraints on the CCSN and LGRB progenitor mass ranges, and test the IMF universality. These results show the potential of this kind of approach for studying the IMF, its putative evolution with the galactic environment and cosmic history, and the properties of SN Ia, CCSN, and LGRB progenitors, especially considering the wealth of data incoming in the future.



Citation: Gabrielli, F.; Boco, L.; Ghirlanda, G.; Salafia, O.S.; Salvaterra, R.; Spera, M.; Lapi, A. Constraining the Initial Mass Function via Stellar Transients. *Universe* **2024**, *10*, 383. <https://doi.org/10.3390/universe10100383>

Academic Editor: Antonino Del Popolo

Received: 11 August 2024

Revised: 13 September 2024

Accepted: 27 September 2024

Published: 29 September 2024



Copyright: © 2024 by the authors. Licensee MDPI, Basel, Switzerland. This article is an open access article distributed under the terms and conditions of the Creative Commons Attribution (CC BY) license (<https://creativecommons.org/licenses/by/4.0/>).

1. Introduction

The stellar initial mass function (IMF) describes the mass distribution of stars in the zero-age main sequence (ZAMS). It plays a pivotal role in many different topics of astrophysics and cosmology, spanning from stellar and binary evolution to galaxy evolution and cosmological reionization. Past and current empirical determinations of the IMF rely

either on the observation of stellar populations inside our Galaxy and in the Local Group or on the study of the suggested correspondence between the IMF and the mass function of observed pre-stellar dense cores (see, e.g., the recent review by [1] and references therein). Regarding the first method, the IMF can be inferred either from direct star counts, in the case of resolved stellar populations, or via careful modeling of, e.g., galaxy spectra or gravitational lensing in the case of unresolved stellar populations (see [1] and references therein). Based on these observational results, a number of parametrizations have been introduced to model the IMF, the most common being those by [2–9]. However, as pointed out, e.g., in [10,11], a large part of IMF measurements underestimate the scatter observed in the IMF slopes, as well as the difficulty in disentangling systematics from physical IMF environmental dependencies. These limitations also threaten the common assumption of an IMF universality, with a number of works suggesting IMF dependence on, e.g., redshift, metallicity, and/or star formation rate (SFR) (e.g., [11–17]). On the theory side, numerous works have tried to explain the physical origin of the IMF characteristic mass, identifying its peak and high-mass slope (see [1] and references therein). Despite all these efforts, many fundamental uncertainties still exist around the properties of the IMF and its physical nature.

The IMF plays a key role in the study of stellar transients since it describes the mass distribution of their progenitors. In particular, it is crucial for computing the cosmic rates of type Ia supernovae (SNe Ia) and core-collapse supernovae (CCSNe). Moreover, the IMF critically determines the amount of UV radiation emitted by stars in galaxies.

Young massive stars are responsible for the emission of ionizing radiation in the UV band. The corresponding UV luminosity density can be computed by integrating UV luminosity functions measured with galaxy surveys (e.g., [18–21]). Since UV light traces the abundance of young massive stars, it is intimately linked to the star formation rate (SFR). Consequently, the cosmic UV luminosity density, $\rho_{UV}(z)$, can be converted to a cosmic star formation rate density (SFRD), $\rho_{SFR}(z)$, which indicates the amount of star-forming mass available at redshift z per unit time and comoving volume. This conversion is recurrently performed using a factor k_{UV} , expressing the efficiency in the production of UV photons from stars. The value of k_{UV} clearly depends on the IMF as the latter determines the relative number of massive stars compared to low-mass ones [22–27].

SNe Ia are thermonuclear transients arising in binary systems composed of at least one white dwarf (WD) from progenitor stars of at least $2–3 M_{\odot}$ (e.g., [28,29]). CCSNe, instead, represent the endpoint of massive star evolution above $\sim 8 M_{\odot}$, and are believed to arise from the collapse of the more external layers of the star onto the iron core and the subsequent neutrino-driven explosion (e.g., [30–34]). Great uncertainties revolve around the upper limit of CCSN progenitors, which might vary in the range of $\sim 20–25 M_{\odot}$ all the way up to $100 M_{\odot}$ (e.g., [35–37]). Indeed, stars inside this mass range are thought to experience fall-back of the ejected material onto the core, giving rise to a faint “failed” SN, and collapse into a BH (e.g., [36–41]). Above $\sim 100 M_{\odot}$, stars develop pair instability inside their core, and end their lives before completing all nuclear burning stages [35,36]. Given the dependence of SNe Ia and CCSNe on the progenitor mass, the IMF explicitly enters in setting their rates.

There exists another class of stellar transients that, differently from SNe Ia and CCSNe, exhibit a crucial dependence on metallicity, i.e., long gamma-ray bursts (LGRBs). According to the “collapsar” scenario, LGRBs arise from the collapse of massive stars, and the formation of an accretion disk around the BH remnant. If the disk is sufficiently massive, and the BH sufficiently spinning, a jet can be launched perpendicularly to the disk, powering the LGRB emission [42]. Host galaxy studies and simulations show an LGRB preference for low-metallicity environments, suggesting the existence of a maximum metallicity above which stars cannot produce these transients (e.g., [36]). A number of LGRBs have been observed in association with type Ib/c SNe, suggesting a shared progenitor (e.g., [43–49]). This might indicate a preferential origin in binary systems, where the progenitor can be stripped of its envelope by means of the companion. All in all, the properties of LGRB pro-

genitors, and especially their mass range, are still unknown. The joint study of LGRBs and the cosmic metallicity (Z) evolution holds the potential to uncover the elusive progenitors of LGRBs, and increase our understanding of galaxy evolution.

As explained above, the IMF is deeply intertwined with both stellar transients and galaxy UV luminosity. Due to the realization of this fil rouge, in this paper, we are motivated to attempt to infer the IMF with a novel method, based on combining observational constraints related to these quantities, in a way that is completely independent from previous IMF determinations.

Specifically, we build a parametric model for the cosmic UV luminosity density, local stellar mass density (SMD), and SN Ia, CCSN, and LGRB rates as a function of redshift, and constrain the model parameters in order to match the observational determinations available for these quantities. We achieve this by employing a Bayesian Markov Chain Monte Carlo method (MCMC). Our approach also allows us to constrain the properties of SN Ia and CCSN progenitors. Moreover, the adoption of an up-to-date recipe for the cosmic metallicity evolution enables us to study the properties of LGRB progenitors. Finally, we explore what the set of observational constraints adopted here can tell us about the putative IMF evolution with redshift, and discuss how variations in our model assumptions can alter our results.

This work is structured as follows: In Section 2, we describe how we compute the different quantities presented above, and introduce the free parameters of our model. Then, we explain the basics of our MCMC, and present our results in Section 3. We discuss our findings in Section 4, as well as some variations in the model assumptions, and, finally, draw our conclusions in Section 5. Throughout this work, we assume a flat Λ CDM cosmology, with parameters $H_0 = 70 \text{ km s}^{-1} \text{ Mpc}^{-1}$, $\Omega_M = 0.3$. We adopt the value of $Z_\odot = 0.0153$ for the Solar metallicity [50], and $12 + \log(\text{O/H})_\odot = 8.76$ for the Solar oxygen abundance. Unless specified otherwise, we consider absolute metallicities.

2. Methods

We follow a parametric, semi-empirical approach in order to model the cosmic UV luminosity density, $\rho_{UV}(z)$, the local SMD, $\rho_{*,0}$, and the SN Ia, CCSN, and LGRB rates as a function of redshift, $R_{Ia}(z)$, $R_{CC}(z)$, $R_{LGRB}(z)$. We then employ a Bayesian MCMC in order to match our model predictions to the data. This allows us to keep the number of physical assumptions to the minimum, and obtain an estimate of the model parameters that is directly informed by observations.

Throughout this work, we assume an IMF with a Larson shape [51],

$$\phi(m) \propto m^\xi e^{-m_c/m}, \quad (1)$$

with free parameters m_c , the characteristic mass, and the slope ξ .

2.1. UV Luminosity Density

The UV luminosity density, $\rho_{UV}(z)$, represents the energy in the UV photons present at a given redshift per unit time and comoving volume, typically expressed in units of $\text{erg s}^{-1} \text{ Mpc}^{-3}$. We adopt a standard [24] functional form,

$$\rho_{UV}(z) = \rho_{UV,0} \frac{(1+z)^\alpha}{[1 + (1+z)/\gamma]^\beta}, \quad (2)$$

where the normalization $\rho_{UV,0}$ is the local UV luminosity density. Based on the assumed IMF, one can convert this quantity to an SFRD via the following equation:

$$\rho_{SFR} = \rho_{UV} / k_{UV}(m_c, \xi), \quad (3)$$

where k_{UV} is the UV photons' production efficiency in units of $\text{erg s}^{-1} \text{ Hz}^{-1} \text{ M}_\odot^{-1} \text{ yr}$. We compute it by employing the PARSEC stellar evolution code [52–60]. In particular, we use

stellar evolution tracks to compute the mean production rate of UV photons, and then average the result over the IMF to obtain k_{UV} . For simplicity, we adopt fixed values for the age and metallicity of the stellar population, 10^9 yr and $Z = 0.02$, respectively. We check that varying the stellar age to 10^8 yr and 10^{10} yr, and the metallicity to $Z = 0.002$ and 0.0002 , has a negligible effect on the results.

In order to fit ρ_{UV} , we consider a set of the most recent SFRD determinations from UV, IR, and submm surveys, including the JWST surveys [19–21,61–68]. We convert ρ_{SFR} to ρ_{UV} via Equation (3) according to the IMF used in these works. We decide to restrict the data to $z < 9$ since, as shown below, the observational constraints on the stellar transient rates employed in this work do not exceed this redshift (in particular, those related to the LGRB rate). This choice also allows us to avoid the uncertainties in the SFRD data at higher redshifts.

2.2. Local Stellar Mass Density

By integrating the SFRD from $z = \infty$ down to a given redshift z , one can compute the total amount of star-forming mass accumulated throughout the whole history of the Universe down to that redshift per unit comoving volume, i.e., the SMD (see, e.g., [24]):

$$\rho_{\star}(z) = (1 - R) \int_{\infty}^z \rho_{SFR}(z) \frac{dt}{dz} dz \quad (4)$$

R accounts for the fraction of stellar mass returned into the ISM or IGM during stellar evolution via winds or SN explosions. We compute it following [24], under the assumption that stars above $1 M_{\odot}$ lose mass the moment they are born (the “instantaneous recycling approximation”):

$$R = \int_{1 M_{\odot}}^{300 M_{\odot}} dm (m - \omega_m) \phi(m), \quad (5)$$

where $\phi(m)$ is the IMF, and the upper limit of integration is the maximum stellar mass considered in this work. ω_m is the remnant mass, which we compute using the initial-final mass relation (IFMR) from [69] for $m > 8 M_{\odot}$ and that from [70–72] for $m < 8 M_{\odot}$. In particular, we consider the result from [69] for $Z = 0.02$. We find that employing the IFMR for $Z = 0.002$ and $Z = 0.0002$ has a negligible effect on the results. The adopted IFMR for $m < 8 M_{\odot}$ is computed at $Z = 0.014$. As discussed, e.g., by [70], the IFMR is not expected to exhibit a crucial dependence on metallicity in this mass range.

In order to obtain an observational constraint on the local SMD, we consider a recent determination of the galaxy stellar mass functions (GSMFs) by [73] based on the COSMOS2020 galaxy catalog. We focus on the results obtained in the lowest redshift bin, $z \sim 0.2$ –0.5. GSMFs represent the number of galaxies per unit stellar mass and comoving volume, $\Phi(M_{\star}) = d^2N/dM_{\star} dV$. By integrating over stellar mass, one can compute the total mass in stars per unit comoving volume, i.e., the SMD:

$$\rho_{\star,0} \equiv \rho_{\star}(z \sim 0.35) = \left(\int dM_{\star} M_{\star} \Phi(M_{\star}) \right) \frac{\langle M_{\star}/L_{UV} \rangle}{\langle M_{\star}/L_{UV} \rangle_{Ch}}, \quad (6)$$

where $z \sim 0.35$ is the mean redshift in the considered bin. The factors on the right of the integral are the stellar mass-to-light ratios, which we use to convert from the Chabrier IMF used in [73] to the IMF adopted here (as performed, e.g., in [24]). We compute these quantities via the PARSEC stellar evolution tracks. Finally, we compare this observational constraint with the SMD from Equation (4), computed at $z = 0.35$.

2.3. Core-Collapse Supernova Rate

Regarding the CCSN rate, we start by computing the number of CCSNe produced per unit of star-forming mass according to the following equation:

$$\frac{dn_{CC}}{dM_{\star}} = \int_{M_{CC}^{low}}^{M_{CC}^{up}} dm \phi(m), \quad (7)$$

where we integrate the IMF over the mass range of the CCSN progenitors. The minimum stellar mass to produce a CCSN, M_{CC}^{low} , is expected to be around $8 M_{\odot}$ (e.g., [36,37]). On the other hand, the upper limit M_{CC}^{up} is highly uncertain (e.g., [35–37]). Based on these considerations, we decide to fix $M_{CC}^{low} = 8 M_{\odot}$, and keep M_{CC}^{up} as a free parameter. Finally, we compute the CCSN rate as a function of redshift as follows:

$$R_{CC}(z) = \frac{dn_{CC}}{dM_{\star}} \times \rho_{SFR}(z) \quad (8)$$

In doing so, we assume no delay between star formation and the CCSN explosion since the corresponding timescale ($\lesssim 100$ Myr) is negligible on cosmological scales.

We compare this to a set of observational determinations of the CCSN rate from the literature, spanning a redshift range up to $z \sim 2.3$ [12,74–87]. This set comprises, to the best of our knowledge, all existing data available for this quantity. All rates are derived for $H_0 = 70 \text{ km s}^{-1} \text{ Mpc}^{-3}$, the same value adopted in this work.

2.4. Type Ia Supernova Rate

SNe Ia are thermonuclear explosions of WDs in binary systems triggered either by accretion from a companion star (the “single-degenerate” scenario, SD) or by a merger with another WD (“double degenerate”, DD). We compute the number of SNe Ia produced per unit of star-forming mass as

$$\frac{dn_{Ia}}{dM_{\star}} = N_{Ia} \int_{M_{Ia}^{low}}^{M_{Ia}^{up}} dm \phi(m). \quad (9)$$

We agnostically account for all effects of binary evolution with the normalization factor N_{Ia} , similarly to, e.g., in [28,82,84,88–93]. N_{Ia} also includes the binary fraction, f_{bin} , i.e., the fraction of stars lying in a binary with respect to the whole stellar population. Then, we integrate the IMF over the expected mass range of SN Ia progenitors. WD progenitors lie at masses starting from ~ 0.7 – $0.8 M_{\odot}$, i.e., the minimum mass for a star to complete the MS, and finally evolve into a WD on a timescale less than the age of the Universe. However, it is believed that, in order for the WD to give rise to an SN Ia, the progenitor star must be at least 2 – $3 M_{\odot}$ (e.g., [28,29]). On the other hand, there is overall consensus placing the upper limit of SN Ia progenitors at $\sim 8 M_{\odot}$ at the onset of core collapse. For these reasons, we fix $M_{Ia}^{low} = 3 M_{\odot}$, and $M_{Ia}^{up} \equiv M_{CC}^{low} = 8 M_{\odot}$. We check that moving M_{Ia}^{low} to $2 M_{\odot}$ does not affect our results significantly. As in the case of CCSNe, we do not consider any dependence on metallicity, a standard assumption (but see, e.g., [94–97], where this assumption is challenged).

Since, differently from CCSNe, the timescales for an SN Ia explosion after the birth of the progenitor star are not negligible, we compute the SN Ia rate by convolving the SFRD with a delay time distribution (DTD), $\Psi(t)$, following [29]:

$$R_{Ia}(z) = \frac{dn_{Ia}}{dM_{\star}} \times \int_{40 \text{ Myr}}^{t(z)} d\tau \rho_{SFR}(t - \tau) \Psi(\tau), \quad (10)$$

where $t(z)$ is the age of the Universe at redshift z , and we choose the lower cut of 40 Myr as the delay time associated with stars of ~ 8 – $10 M_{\odot}$. We adopt a DTD of the form $\propto t^{-1}$ following [29,98] and the references therein.

We match this theoretical SN Ia rate to a set of observational determinations from the literature, reaching up to $z \sim 2.3$ [74–76,78,79,82,84,85,90,99–130]. This set represents, to the best of our knowledge, all existing data available for this quantity. All rates are derived for $H_0 = 70 \text{ km s}^{-1} \text{ Mpc}^{-3}$, the same value adopted in this work.

2.5. Long Gamma-Ray Burst Rate

In order to model the LGRB rate, we first compute the number of LGRBs produced per unit of star-forming mass, dn_{LGRB}/dM_* , as follows:

$$\frac{dn_{LGRB}}{dM_*}(Z) = \begin{cases} N_{LGRB} \int_{M_{LGRB}^{low}}^{M_{LGRB}^{up}} dm \phi(m) & \text{if } Z \leq Z_{max}, \\ 0 & \text{if } Z > Z_{max}. \end{cases} \quad (11)$$

Here, we integrate the IMF over the mass range of LGRB progenitors, and ascribe all uncertainties related to, e.g., progenitor rotation, jet-launching conditions, and LGRB emission to a normalization factor N_{LGRB} in front of the integral. In addition, we implement a dependence of dn_{LGRB}/dM_* on metallicity by defining a maximum metallicity Z_{max} above which LGRBs are suppressed. Indeed, the higher the progenitor metallicity, the more mass and angular momentum will be lost via stellar winds. Given that the remnant rotation must be high enough to launch the relativistic jet, too high metallicities hinder LGRB emission (e.g., [131–135]).

Since LGRB occurrence depends on the metallicity of the environment where their progenitors form, their study requires a treatment of the galaxy metallicity evolution throughout cosmic history. We resort to a fundamental metallicity relation (FMR), $Z_{FMR}(M_*, \psi)$, linking galaxy metallicity to stellar mass and SFR, ψ . In particular, we consider the recent determination by [136], taking also into account the offset from the FMR found in [137] above $z \sim 3$ (we fit their results with a simple power-law function). Due to the intrinsic dependencies of Z_{FMR} on M_* and ψ , we build the Z -dependent SFRD by convolving GSMFs with a galaxy main sequence (MS), relating stellar mass and SFR according to the following equation (see also [138]):

$$\begin{aligned} \frac{d^3 M_{SFR}}{dt dV d \log Z}(Z, z) &= \int d \log M_* \frac{d^2 N}{dV d \log M_*}(M_*, z) \\ &\times \int d \log \psi \psi \frac{dp}{d \log \psi}(\psi, M_*, z) \\ &\times \frac{dp}{d \log Z}(Z, Z_{FMR}(M_*, \psi), \sigma_Z). \end{aligned} \quad (12)$$

For coherence with our SMD computation, we consider the GSMFs by [73], while, for the MS, we follow [139]. $dp/d \log \psi$ is a log-normal SFR distribution, accounting for both MS and starburst galaxies (SBs). The latter are galaxies with a particularly high SFR which identify a separate region above the MS in the M_* – ψ plane. We treat SBs following [140]. $dp/d \log Z(Z, Z_{FMR}, \sigma_Z)$ describes a log-normal Z distribution around the FMR with dispersion σ_Z .

We then use the result from Equation (12) to compute the fraction of star formation taking place below a certain metallicity at a given redshift, F , as follows:

$$F(z, Z_{max}, \sigma_Z) = \frac{\int_{-\infty}^{\log Z_{max}} d \log Z \frac{d^3 M_{SFR}}{dt dV d \log Z}(Z, z)}{\int d \log Z \frac{d^3 M_{SFR}}{dt dV d \log Z}(Z, z)}. \quad (13)$$

F not only depends on redshift and Z_{max} , but also on the parameter σ_Z , i.e., the dispersion in the galaxy metallicity distribution (entering $dp/d \log Z$ in Equation (12)).

We finally compute the LGRB rate as a function of redshift as follows:

$$R_{LGRB}(z) = \frac{dn_{LGRB}}{dM_*} \times F(z, Z_{max}, \sigma_Z) \rho_{SFR}(z), \quad (14)$$

where $\rho_{SFR}(z)$ is the SFRD from Equation (3).

Inferring the LGRB intrinsic rate from observations is more complex than in the case of SNe Ia and CCSNe. Indeed, after the computation of the observed rate from the data, some additional observational biases must be addressed (see, e.g., [141]). On the one hand, only LGRBs with jets oriented towards our line of sight can be observed. In order to account for the off-axis population, a correction based on the jet opening angle is required. Moreover, LGRBs are detected up to much higher redshifts than SNe Ia and CCSNe; thus, a fraction of the population will inevitably be too faint to be detected with a given instrument. One can overcome this bias by assuming an underlying LGRB luminosity function and integrating it below the detection threshold of the instrument. Noticeably, [142] derives the intrinsic LGRB rate and luminosity function as a function of redshift by simulating a population of sources with randomly oriented jets and matching the predictions of their model to several datasets of LGRB observables. These comprise peak flux and energy, fluence, duration, redshift, isotropic equivalent luminosity and energy, and jet opening angle distributions. They also account, for the first time in an LGRB population study, for relativistic effects due to the jet orientation and beaming. We decide to adopt an updated version of their LGRB rate determination, taking into account more recent observations of LGRBs at high redshift (see Appendix A) to match the outcome of our model.

2.6. MCMC

We perform an MCMC by using the Python package (version 3.12.3) *emcee* (<https://emcee.readthedocs.io/en/stable/>), accessed on 25 September 2024 [23]), selecting 2×10^2 walkers. The number of steps needed for the MCMC to converge is approximately 4×10^4 . There are 13 free parameters to be constrained: $\theta = [\log \rho_{UV,0}, \alpha, \beta, \gamma, \log m_c, \xi, \log N_{Ia}, \log M_{CC}^{up}, \sigma_Z, \log N_{LGRB}, \log Z_{max}, \log M_{LGRB}^{low}, \log M_{LGRB}^{up}]$. The first four parameters define the shape and normalization of $\rho_{UV}(z)$; N_{Ia} is the fraction of stars in the mass range of SN Ia progenitors that actually give rise to an SN Ia; M_{CC}^{up} is the maximum CCSN progenitor mass; and $\log m_c$ and ξ are the IMF characteristic mass and slope. The last five parameters are instead related to the metallicity evolution and the properties of LGRB progenitors: σ_Z represents the dispersion of the galaxy metallicity distribution; N_{LGRB} is the fraction of stars with a mass in the range of LGRB progenitors that produce a successful LGRB emission; Z_{max} is the maximum metallicity for LGRBs; and $M_{LGRB}^{low/up}$ set the mass range of LGRB progenitors. We define uniform priors in the ranges $\log \rho_{UV,0} = [25, 26.5]$, $\alpha = [0, 7]$, $\beta = [4, 10]$, $\gamma = [0, 5]$, $\log m_c = [-2, 2]$, $\xi = [-5, 0]$, $\log N_{Ia} = [-3, 0]$, $\log M_{CC}^{up} = [\log(10), \log(150)]$, $\sigma_Z = [0, 1]$, $\log N_{LGRB} = [-3, 0]$, $\log Z_{max} = [-4, -1]$, $\log M_{LGRB}^{low} = [\log(10), \log(150)]$, $\log M_{LGRB}^{up} = [\log(10), \log(150)]$. For every observable O , we then compute the logarithmic likelihood as follows:

$$\ln \mathcal{L}_O(\theta) = -\frac{1}{2} \sum_i \left[\frac{(O(z_i, \theta) - D_i)^2}{s_i^2} + \ln(2\pi s_i^2) \right], \quad (15)$$

where the sum runs over the redshifts z_i of the corresponding data points. $O(z_i, \theta)$ is the model observable computed at z_i for a given choice of parameters θ , while D_i is the i -th data point. In the additional term inside the sum, $s_i^2 = \sigma_i^2 + O(z_i, \theta)^2 e^{2\ln f}$, where σ_i is the uncertainty associated with D_i . f is an additional free parameter that takes into account possible systematics in the data. We allow $\ln f$ to vary uniformly in $[-10, 1]$. According to the Bayes theorem, the posterior probability for the choice of parameters θ can be computed as $\log P(\theta) = \log p(\theta) + \sum_O \log \mathcal{L}_O(\theta)$, where $\log p(\theta)$ is 0 if all parameters are within their prior ranges; otherwise, it returns $-\infty$. The MCMC takes these quantities as input and computes the best fit for the model parameters, as well as their marginal and joint posterior probability distributions. We plot the latter quantities via the Python package *GetDist* (<https://getdist.readthedocs.io/en/latest/>), accessed on 25 September 2024). As explained in Section 2.5, due to the complex observational biases linked to LGRB detection, we consider the determination of the LGRB rate as a function of redshift following [142] (more specifically, an updated version of their result; see Appendix A). For this reason,

we compute the likelihood terms related to LGRBs following a conceptually different, but formally identical, approach. In particular, from the updated LGRB rate determination by [142], we only sample 10 points, uniformly spaced in cosmic age. By doing so, we take into account the fact that the number of LGRB observations decreases when going to higher redshift, with only a few LGRB detections achieved so far at very high redshift (e.g., $z > 6$). We then define Gaussian priors around each of these points, with errors equal to the 1σ uncertainty of the LGRB rate determination at the corresponding redshifts. The constraints informed by these priors allow us to estimate the model parameters. We stress that the posterior probability computed in this way is mathematically identical to that shown above, i.e., $\log P(\theta) = \log p(\theta) + \sum_O \log \mathcal{L}_O(\theta)$ and Equation (15), since the additional terms of the Gaussian priors are the same as those in Equation (15). Therefore, the computation of the posterior probability for the parameter space describing LGRBs and the cosmic metallicity evolution is fully consistent with that for the UV luminosity density, local SMD, SN Ia, and CCSN rate parameters.

3. Results

In this section, we present the results obtained in this work. Our result for the IMF is displayed in Figure 1. We find the parameters related to LGRBs and the cosmic Z evolution to be somewhat disentangled from the rest of the parameter space. In particular, the IMF estimate is fully determined by the UV luminosity density, local SMD, SN Ia, and CCSN rates, and does not require LGRBs to be considered as well. On the other hand, adding the latter transients allows us to also put constraints on the LGRB progenitor properties and the cosmic Z evolution. For this reason, and for more clarity, we present separately the results obtained for the parameters related to $\rho_{UV}(z)$, $\rho_{*,0}$, $R_{Ia}(z)$, and $R_{CC}(z)$ (Section 3.1, Figure 2) and those for $R_{LGRB}(z)$ and the cosmic Z evolution (Section 3.2, Figure 4). For completeness, we also report in Appendix B a corner plot with all posteriors found by the MCMC for the whole parameter space (Figure A2). See Table 1 for the median values obtained for all parameters with 1σ uncertainties. The total reduced chi square amounts to $\chi^2_{red} = 1.17$. In Figures 3 and 5, we show the fits obtained for $\rho_{UV}(z)$, $\rho_{*,0}$, $R_{CC}(z)$, $R_{Ia}(z)$, and $R_{LGRB}(z)$ in comparison with the corresponding datasets. Finally, in Section 3.3, we test the assumption of IMF evolution with z .

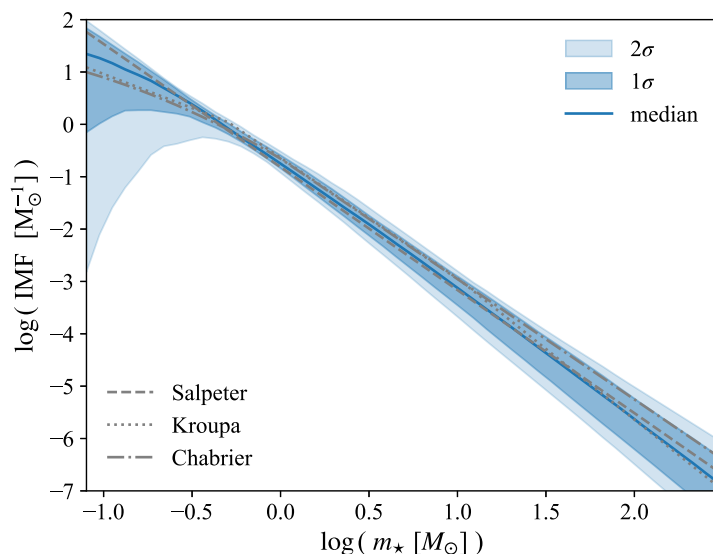


Figure 1. Initial-mass function (IMF) fit as a function of stellar mass. We show the median of the posterior distributions with a blue solid line, as well as the 1σ and 2σ uncertainty bands around the median. For comparison, we plot the Salpeter, Kroupa, and Chabrier IMFs as gray lines.

3.1. Stellar Initial Mass Function, Type Ia Supernovae, and Core-Collapse Supernovae

Our method allows us to obtain for the first time an IMF determination based on the observed rates of stellar transients. We infer an IMF with characteristic mass $\log m_c = -0.99^{+0.52}_{-0.77}$ (i.e., $m_c = 0.10^{+0.24}_{-0.08} M_\odot$) and slope $\xi = -2.53^{+0.24}_{-0.27}$. The IMF slope is remarkably compatible with those typically adopted based on the observed stellar populations in the local Universe. One can see this agreement in Figure 1, where we show our result in comparison with the Salpeter ($\xi = -2.35$, [2]), Kroupa ($\xi = -2.3, -2.7$, [4,6,8]), and Chabrier IMFs ($\xi = -2.3$, [7]). We note that the uncertainties in $\log m_c$ only enlarge the error band at $\log m_c \lesssim -0.5$, a mass range poorly constrained also by local IMF determinations.

As one can see in Figure 2, the ρ_{UV} parameters are particularly well constrained due to the relatively small uncertainties of the corresponding data, at least at low redshift. The larger scatter and error bars of the SN Ia and CCSN rate data points raise the uncertainties for the other parameters. This combines with the fact that, as described in Section 2, their computation requires the conversion from ρ_{UV} to ρ_{SFR} , and the inclusion of the IMF. The quantities the MCMC struggles the most to constrain are $\log m_c$ and $\log M_{CC}^{up}$. This is to be expected since we are only able to survey stellar masses down to $3 M_\odot$, i.e., the assumed minimum mass of SN Ia progenitors, while we cannot put any constraint at lower masses. Moreover, the high-mass end of the IMF is only covered by the CCSN and LGRB rate, for which we have a less constraining dataset. Nonetheless, we retrieve estimates also for these quantities, albeit with larger error bars. In particular, we find $\log M_{CC}^{up} = 1.76 \pm 0.22 M_\odot$ at 1σ confidence level. This means a range of $\sim [35-95] M_\odot$ and a median value of $\sim 58 M_\odot$. Finally, we obtain an estimate for the fraction of SN Ia progenitors that actually produce an SN Ia of $\log N_{Ia} = -1.45^{+0.10}_{-0.13}$, or $N_{Ia} = 3.5 \pm 0.9 \times 10^{-2}$ in non-logarithmic values.

As shown in Figure 3a, we obtain a ρ_{UV} fit peaking at $z \gtrsim 2$. One can notice how our fit does not intercept some of the data points, which, indeed, exhibit a significant scatter. This is possibly due to the fact that we combine data from several works that are independent from each other and are obtained from different galaxy surveys in different bands. As explained in Section 2.6, we account for the possible resulting systematics via an additional parameter f in the computation of the likelihood, the value of which is estimated by the MCMC. The same also applies to our results on the CCSN and SN Ia rates (Figure 3c,d), which are similarly based on datasets from different works obtained from independent surveys.

Figure 3b shows the fit we obtain for the local SMD. More specifically, the quantity we consider in this plot is the local SMD divided by the mass-to-light ratio, $\langle M_\star / L_{UV} \rangle$, from Equation (6). In this way, we bring all quantities that depend on the IMF parameters onto one side of the equation and leave only the observational constraint on the other side (see Section 2.2). We indicate the latter with a purple line and error band. We also show $\rho_{\star,0} / \langle M_\star / L_{UV} \rangle$ as a function of $\log m_c$ for three fixed IMF slopes, indicated with gray lines. As one can see, our fit appears to be systematically higher than the data. This is a manifestation of the well-known mismatch between these two SMD determinations, for which an explanation is yet to be found (see, e.g., [24] and references therein). Nonetheless, this comparison is enough for us to constrain the IMF, and, in particular, its slope. Indeed, the plot clearly shows how shallow slopes lead to $\rho_{\star,0} / \langle M_\star / L_{UV} \rangle$ values which are too high with respect to the empirical constraint and are thus excluded. Only slopes $\xi < -2$ are allowed. See Section 4.1 for a deeper discussion about this aspect.

Despite the SN Ia and CCSN data points displaying relatively large error bars, we are still able to constrain the rates of these transients to good accuracy thanks to the interlink with ρ_{UV} . As shown in Figure 3c, R_{CC} peaks at $z \gtrsim 2$, resembling ρ_{UV} . Indeed, we are reminded that R_{CC} is simply a re-normalized ρ_{SFR} , the multiplication factor being dn_{CC} / dM_\star (Equation (8)). On the contrary, as described in Section 2, the computation of R_{Ia} involves the adoption of a DTD. As a consequence, R_{Ia} peaks at lower redshift, closer

to $z = 1.5$ (Figure 3d). One can notice how, in both cases, the error bands become wider at increasing redshifts, where the data are more sparse and uncertain.

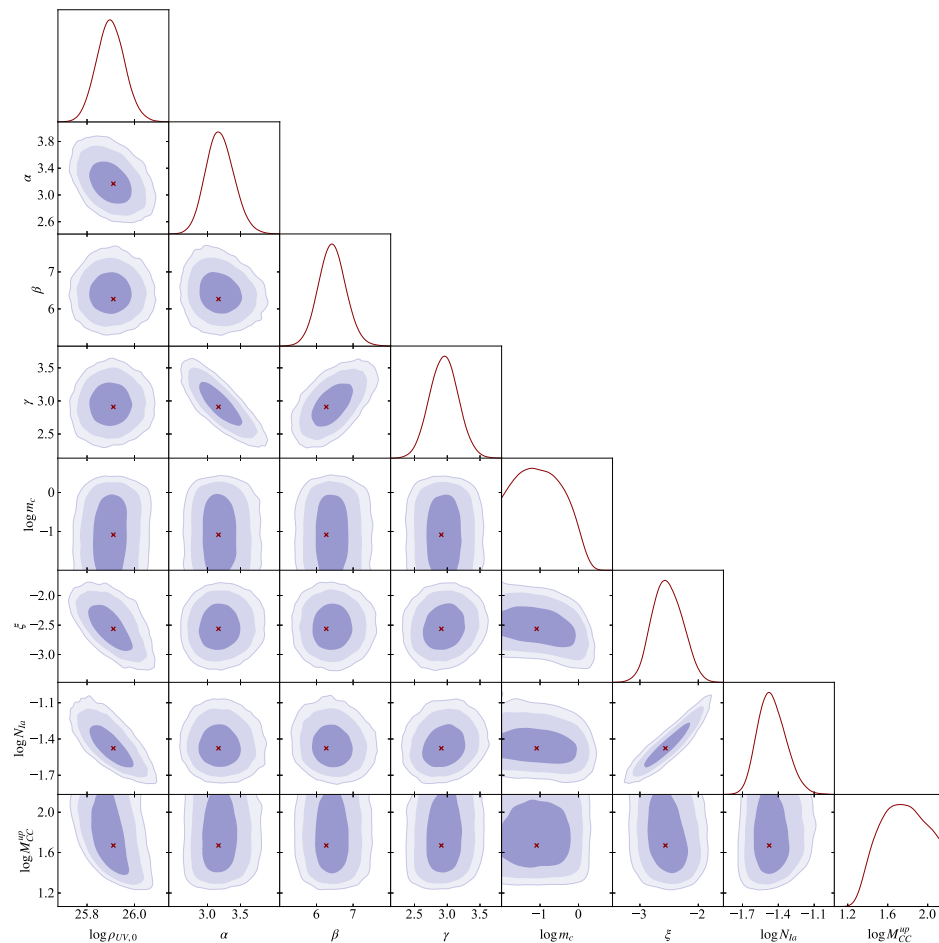


Figure 2. Corner plot showing the individual and joint posterior probability distributions only for the parameters related to ρ_{UV} , $\rho_{*,0}$, R_{Ia} , and R_{CC} , including the IMF parameters $\log m_c$ and ξ . We show the 1, 2, and 3σ confidence level regions in progressively lighter shades. The best-fit values are shown as red crosses.

Finally, we find relevant degeneracies between parameters $\rho_{UV,0}$, ξ , and $\log N_{Ia}$. The correlation between ξ and $\log N_{Ia}$ can be explained with the fact that higher ξ s decrease the number of stars in the range of SN Ia progenitors, between 3 and $8 M_{\odot}$. As a consequence, N_{Ia} must increase in order to meet the observational constraints on R_{Ia} . Moreover, increasing $\rho_{UV,0}$ makes it necessary to decrease $\log N_{Ia}$, and therefore also ξ , to avoid producing too many SN Ia events.

It is important to stress that $\rho_{UV}(z)$, $\rho_{*,0}$, $R_{Ia}(z)$, and $R_{CC}(z)$ are sufficient to provide a robust IMF determination without the need to resort to LGRBs and the metallicity evolution formalism. Indeed, by running the MCMC without the set of constraints on $R_{LGRB}(z)$, we obtain an IMF compatible with that presented in this section with parameters $\log m_c = -0.95^{+0.39}_{-0.98}$ and $\xi = -2.71^{+0.30}_{-0.33}$. We report the posterior distributions obtained in this case in Appendix B (Figure A3), as well as the parameter estimates (Table A1), for completeness. The reduced chi square is $\chi^2_{red} \sim 1.25$, similar to the case with LGRBs.

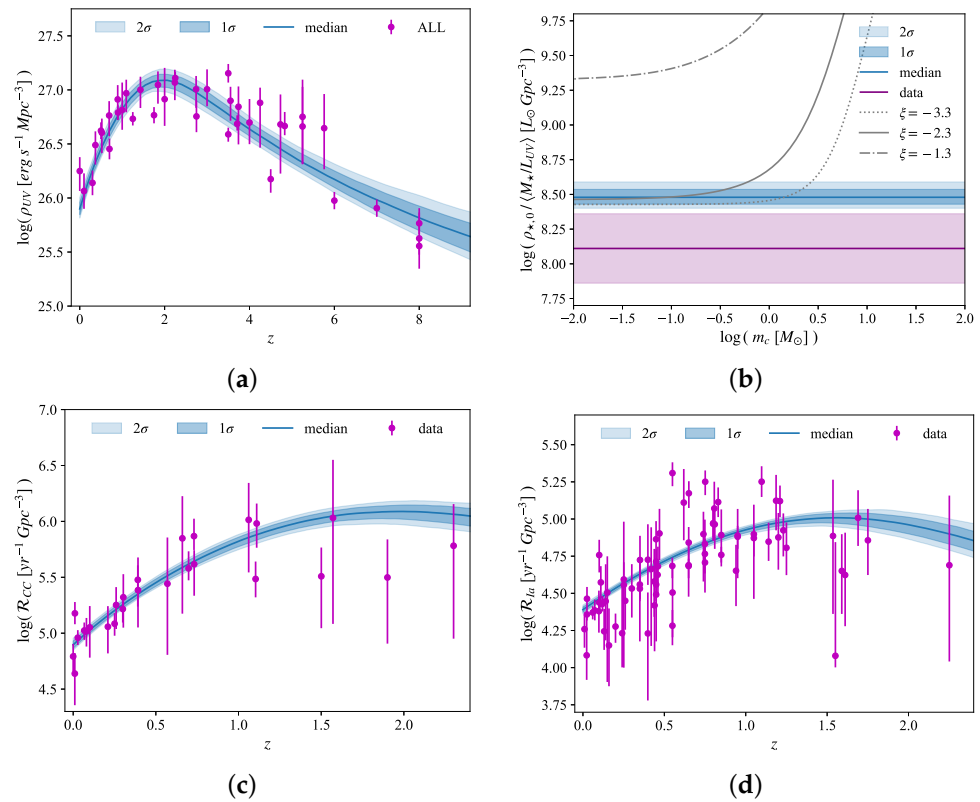


Figure 3. Fits obtained for the UV luminosity density, local stellar mass density (SMD), core-collapse supernova (CCSN), and type Ia supernova (SN Ia) rates as function of redshift compared with the corresponding observational determinations (purple dots and error bars). The blue line and bands show the median and 1σ percentiles of the posterior distribution. (a) UV luminosity density fit as function of redshift. The data points are from [19–21, 61–68]. (b) Local SMD fit, compared with the observational determination obtained from [73]. (c) CCSN rate fit as function of redshift. The data points are from [12, 74–87]. (d) SN Ia rate fit as function of redshift. The data points are from [74–76, 78, 79, 82, 84, 85, 90, 99–130].

3.2. Long Gamma-Ray Bursts and Cosmic Metallicity Evolution

In Figure 4, we show the MCMC results for the parameter space describing LGRB progenitors and the cosmic Z evolution. Noticeably, we find an interplay between the maximum metallicity of LGRB progenitors, Z_{max} , and the dispersion of the galaxy Z distribution, σ_Z . In particular, the smaller σ_Z is, the higher Z_{max} must be in order to provide a sufficient LGRB rate to match the observations. We are able to constrain $\sigma_Z = 0.49^{+0.17}_{-0.27}$ and $\log Z_{max} = -2.75^{+0.54}_{-0.24}$. In non-logarithmic values, $Z_{max} = 1.8^{+4.4}_{-0.8} \times 10^{-3}$. Moreover, we find $\log N_{LGRB} = -0.99 \pm 0.51$, meaning that a median of $\sim 10\%$, and from $\sim 3\%$ to 33% at 1σ level, of stars in the mass range of LGRB progenitors satisfy the conditions for LGRB emission. Regarding the mass range of LGRB progenitors, the MCMC is only able to retrieve $\log M_{LGRB}^{low} < 1.38$ and $\log M_{LGRB}^{up} > 1.71$ (at 1σ), corresponding to $\sim M_{LGRB}^{low} < 24 \text{ M}_\odot$ and $M_{LGRB}^{up} > 51 \text{ M}_\odot$.

As one can see from Figure 5, the 1σ uncertainty on the LGRB rate fit is somewhat larger than for the quantities showed above, reflecting the uncertainties in the parameter estimates. This is mainly due to the dearth of observational constraints at high redshifts. The LGRB rate peaks between $z = 2$ and 3 , higher than the ρ_{UV} peak (Figure 3a). Indeed, according to our model, Z_{max} completely cuts the Z -dependent SFRD distribution above its value, with the effect of shifting the position of the SFRD peak to higher redshifts. See also [143], where this effect is discussed in depth, for the cosmic rate of pair-instability supernovae.

As already pointed out, we find Z_{max} to anti-correlate with σ_Z . Moreover, $\log N_{LGRB}$ correlates with $\log M_{LGRB}^{low}$, since increasing the lower limit on the mass of LGRB progenitors reduces the value of the integral in Equation (14), requiring a higher $\log N_{LGRB}$.

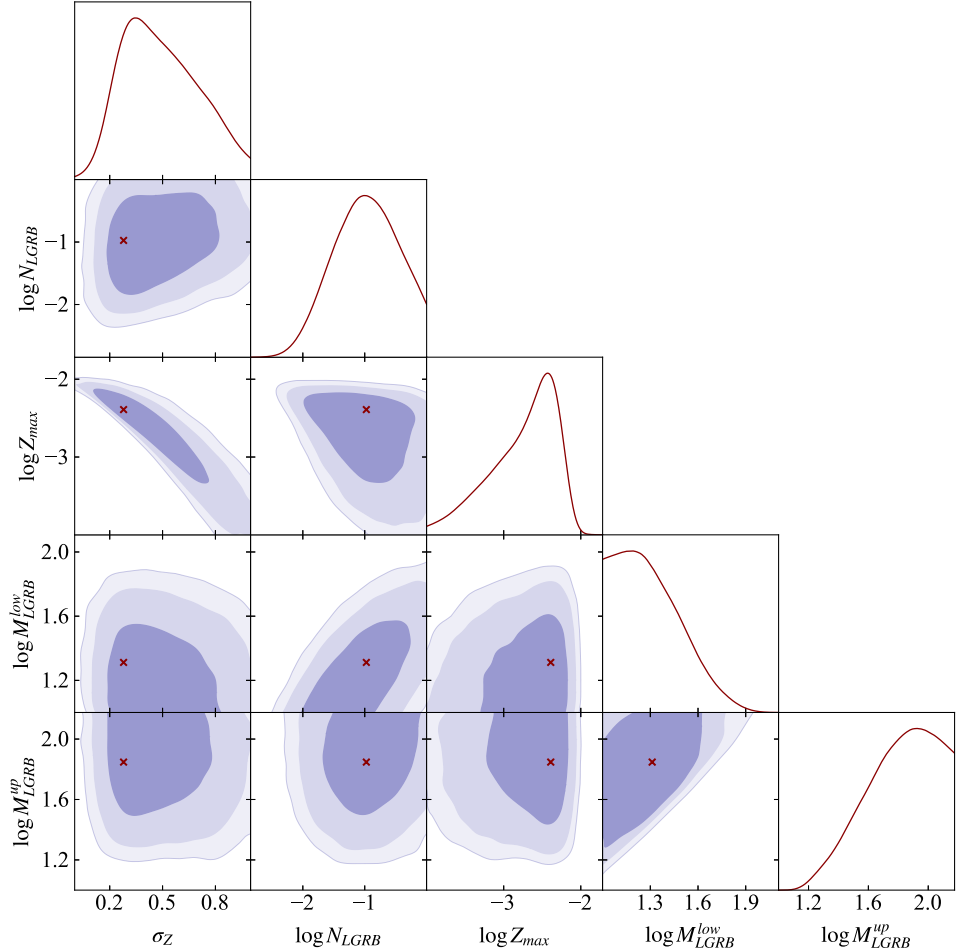


Figure 4. Same as Figure 2 only for the parameters related to R_{LGRB} and the cosmic Z evolution.

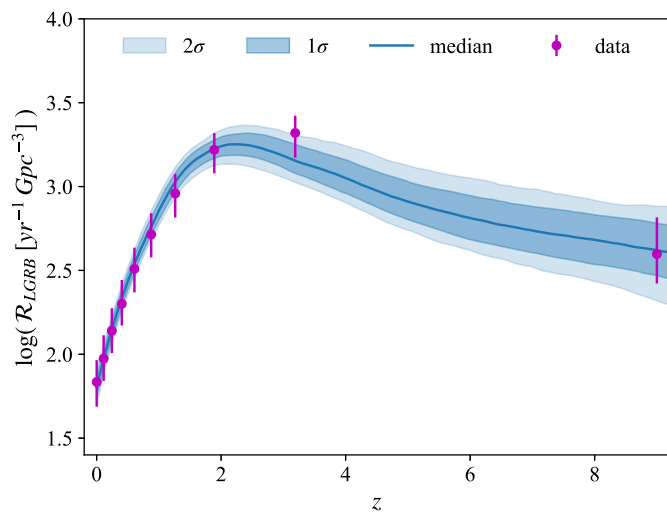


Figure 5. Long gamma-ray burst (LGRB) rate fit as a function of redshift compared to the constraints from [142], updated as described in the Appendix (purple dots and error bars). We show the median and $1, 2\sigma$ percentiles with a blue line and bands.

Table 1. Estimates of the model parameters obtained by combining the observational determinations for $\rho_{UV}(z)$, $\rho_{*,0}$, $R_{CC}(z)$, $R_{Ia}(z)$, and $R_{LGRB}(z)$. The errors represent the 1σ uncertainties. We also report the corresponding units in the third column, where dashes indicate dimensionless quantities.

		$\log(\text{erg s}^{-1} \text{Mpc}^{-3})$
$\log \rho_{UV,0}$	25.90 ± 0.06	
α	$3.19^{+0.20}_{-0.23}$	-
β	6.43 ± 0.38	-
γ	2.95 ± 0.22	-
$\log m_c$	$-0.99^{+0.52}_{-0.77}$	$\log(M_\odot)$
ξ	$-2.53^{+0.24}_{-0.27}$	-
$\log N_{Ia}$	$-1.45^{+0.10}_{-0.13}$	-
$\log M_{CC}^{up}$	1.76 ± 0.22	$\log(M_\odot)$
σ_Z	$0.49^{+0.17}_{-0.27}$	-
$\log N_{LGRB}$	-0.99 ± 0.51	-
$\log Z_{max}$	$-2.75^{+0.54}_{-0.24}$	-
$\log M_{LGRB}^{low}$	<1.38	$\log(M_\odot)$
$\log M_{LGRB}^{up}$	>1.71	$\log(M_\odot)$
$\ln f$	$-4.39^{+0.22}_{-0.18}$	-

3.3. IMF Evolution with Redshift

As explained above, in this work, we make the assumption of a universal IMF, independent from, e.g., redshift, metallicity, or SFR. In this section, we suspend this assumption, and explore whether the observational constraints employed in this work can provide any indication of an IMF evolution with redshift.

We prescribe a redshift dependence for both the IMF characteristic mass and slope. For the former, we adopt a simple power-law dependence, following [144]:

$$m_c(z) = m_{c,0} (1+z)^\gamma, \quad (16)$$

where $m_{c,0}$ is the IMF characteristic mass at $z = 0$, and γ describes the evolution with redshift. We instead parametrize the evolution of the IMF slope as in [145]:

$$\xi(z) = \begin{cases} \xi_0 & \text{if } z < z_0 \\ \xi_0 - f_{imf}(z - z_0) & \text{if } z \geq z_0, \end{cases} \quad (17)$$

where ξ_0 is the IMF slope at $z = 0$, and z_0 is the redshift at which the slope begins to vary. We implement this redshift dependence in the computation of all quantities presented in Section 2, leading to $\rho_{UV}(z)$, $\rho_{*,0}$, $R_{Ia}(z)$, $R_{CC}(z)$, and $R_{LGRB}(z)$. Finally, we run the MCMC with the additional free parameters $[m_{c,0}, \xi_0, \gamma_{imf}, f_{imf}, z_0]$, where we substitute m_c from the previous sections with $m_{c,0}$ and ξ with ξ_0 . Thus, we end up with a total of 16 free parameters, plus the factor $\ln f$ from Section 2.6. We note right away that we are also trying to run the MCMC with $m_c(z)$ being variable and ξ fixed, and with m_c being fixed and $\xi(z)$ variable, but we obtain similar results as in the case where both parameters are variable. Thus, we only report the results for the latter case.

Figure 6 shows the IMF fit we obtain at $z = 0$, $z = 4$, and $z = 9$ in order to show the IMF dependence on redshift. In Figure 7, we show the posterior probabilities we obtain for the parameter space related to the IMF evolution, while, in Table 2, we report the corresponding parameter estimates. For the complete corner plot over the whole parameter space, and the table with all parameter estimates, see Appendix C. The reduced chi square is $\chi^2_{red} \sim 1.25$, similar to that obtained in the case of a universal IMF.

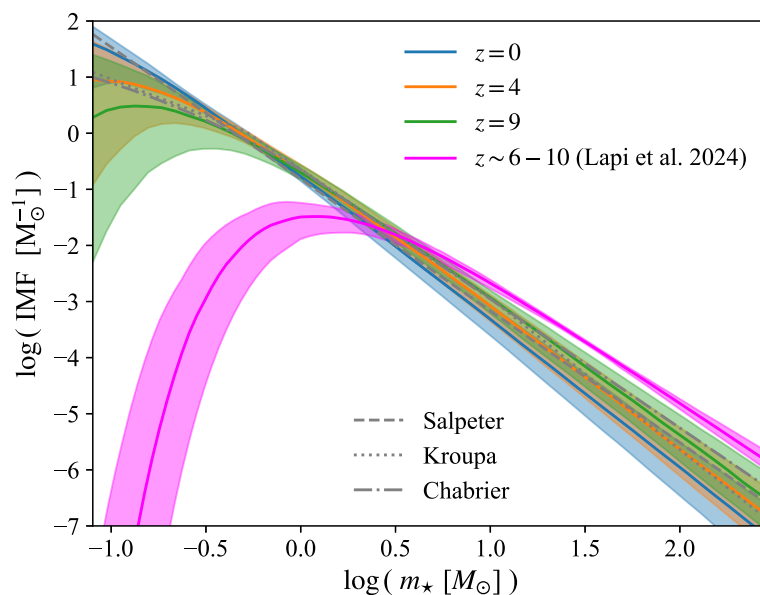


Figure 6. IMF fit as a function of stellar mass obtained in the case of variable IMF with redshift. In order to show the IMF evolution, we plot the results obtained for $z = 0$, $z = 4$, and $z = 9$ (blue, orange, and green lines, respectively). Solid lines indicate the median of the posterior distributions, while the shaded areas correspond to the 1σ errors. For comparison, we plot the Salpeter, Kroupa, and Chabrier IMFs as gray lines. We also show the IMF at the epoch of reionization ($z \sim 6-10$) derived in [146], assuming the [147] escape fraction of ionizing photons. See the text for a comparison with our results.

According to our results, the IMF slope appears to be non-evolving with redshift, with an estimate of $f_{imf} < 0.026$ at 1σ confidence level. The parameter z_0 instead remains unconstrained. On the other hand, the estimate we find for $\gamma_{imf} = 0.53_{-0.43}^{+0.21}$ indicates a mild evolution of the IMF characteristic mass with redshift. Both slope and characteristic mass estimates at $z = 0$, $\zeta_0 = -2.55_{-0.29}^{+0.25}$, and $\log m_{c,0} = -1.08 \pm 0.51$ are compatible with those obtained assuming a universal IMF. The same is valid also for the other parameter estimates; see Figure A4 and Table A2 in Appendix C.

In Figure 6, we also show the result for the IMF at the epoch of reionization, i.e., $z \sim 6-10$ from [146], obtained by combining constraints from astrophysical and cosmological data. In particular, we report their result for the [147] escape fraction of ionizing photons. Our IMF slopes are compatible, and we agree in finding no evidence of evolution for this parameter. On the other hand, the [146] IMF exhibits a significantly higher characteristic mass than that found here. We stress that the set of observational constraints adopted in this work is not enough to make an accurate assessment regarding the IMF evolution with redshift. In particular, we are not able to sample low masses relevant to constraining m_c , especially at high redshifts where we only have LGRB data. On the other hand, ref. [146] focuses on the reionization redshifts $z \sim 6-10$, where they impose more robust and stringent constraints. Therefore, this comparison is not meant to be rigorous, and should be taken with caution.

Despite the uncertainties highlighted above, this exploration shows that it might be possible in the future to use this approach to further study the IMF evolution throughout cosmic history, and/or the galactic environment, thanks to more and more constraining data.

4. Discussion

4.1. Initial Mass Function

In this work, we find that the observational constraints coming from the UV luminosity density, the local SMD and the SN Ia and CCSN rates as a function of redshift allow us to obtain a new determination of the stellar IMF. Remarkably, our result is compatible with the most common IMFs traditionally assumed, inferred from stellar observations in the local Universe, e.g., the Salpeter, Kroupa, and Chabrier IMFs. This might indicate that these IMFs describe stellar populations not only locally, but at least up to Cosmic Noon (i.e., $z \sim 2-3$), up to which we have SN Ia and CCSN rate data. Since we do not make any assumption for the IMF outside of a flexible Larson-shaped parametrization, our result is directly informed by the observed stellar transient rates.

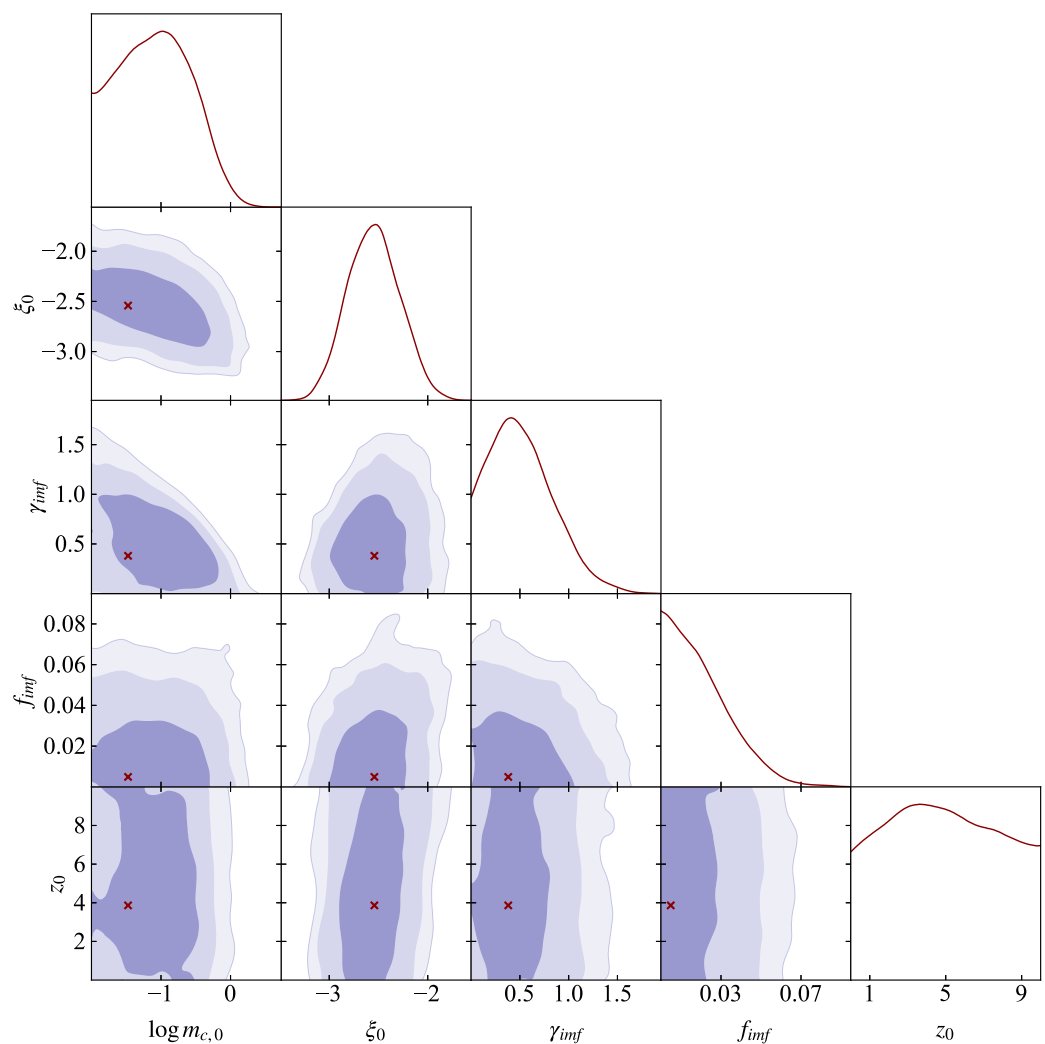


Figure 7. Corner plot with individual and joint posterior probabilities obtained in the case of variable IMF with redshift only for the subset of the parameter space describing the IMF and its evolution. For other details, see the caption of Figure 2.

We find the local SMD to play an important role in constraining the IMF, as can be appreciated by looking at Figure 3b. As one can see, shallow slopes are excluded since they produce too high $\rho_{*,0}/\langle M_*/L_{UV} \rangle$ values. This limits it to slopes $\xi \lesssim -2$. If we remove the constraint on the local SMD, a second peak appears in the ξ posterior distribution. The original peak remains around $\xi \sim -2.5$, while the second one lies around $\xi \sim -1.5$. We believe the latter to be a non-physical solution allowed by the data. Including the local SMD in our dataset completely eliminates this solution. Indeed, while shallower IMF slopes

increase k_{UV} , leading to lower SFRD (Equation (3)) and lower local SMD (Equation (4)), the mass-to-light ratio $\langle M_\star / L_{UV} \rangle$ decreases more steeply for $\xi \gtrsim -2$. As a consequence, $\rho_{\star,0} / \langle M_\star / L_{UV} \rangle$ starts to rapidly increase at $\xi \gtrsim -2$, becoming too high with respect to the observational constraint (Equation (6), where we moved $\langle M_\star / L_{UV} \rangle$ to the other side of the equation). The result is that IMFs with a slope below ~ -2 are ruled out.

Table 2. Estimates of the parameters describing the IMF evolution obtained by implementing an IMF dependence on redshift. The errors represent the 1σ uncertainties. The third column reports the corresponding units, where dashes indicate dimensionless quantities. Note how the parameter z_0 remains unconstrained by the MCMC.

		log(M _⊙)
$\log m_{c,0}$	-1.08 ± 0.51	-
ξ_0	$-2.55^{+0.25}_{-0.29}$	-
γ_{imf}	$0.53^{+0.21}_{-0.43}$	-
f_{imf}	< 0.026	-
z_0	-	-

By adopting a constant IMF, we are assuming that the IMF is universal throughout the redshift range considered in this work. This is a common approximation, despite a number of works exploring the IMF dependence on the environment, e.g., redshift, metallicity, and SFR (e.g., [11–17]). The fact that we obtain an IMF compatible with local stellar observations might support the IMF universality. In order to further explore this point, we try to implement a redshift dependence for the IMF and see if the MCMC can find any evidence of evolution. We find that the observables employed here do not support any significant variation of the IMF slope with redshift. On the other hand, they indicate a mild increase in the IMF characteristic mass with redshift. The uncertainties of the datasets we employ, and the dearth of constraints at high redshift, prevent us from saying anything more about the IMF evolution. Nonetheless, our results show how this treatment could enable us to obtain more stringent constraints in the future, when many more observations will be available.

4.2. Type Ia and Core-Collapse Supernova Progenitors

As described in Section 2, in order to be able to constrain the IMF and the other parameters of interest, we decide to agnostically account for all uncertainties related to the binary nature of SNe Ia with a constant factor N_{Ia} in front of the IMF integral in Equation (9). N_{Ia} represents the fraction of stars with progenitor mass in the range for SNe Ia which actually explode as SNe Ia. It also agnostically accounts for the fraction of stars lying in binaries, f_{bin} . We find $N_{Ia} = 3.5 \pm 0.9 \times 10^{-2}$, meaning that roughly 2 to 5% of stars give rise to SNe Ia given that their mass is in the SN Ia progenitor range. As already shown in Section 3, $\log N_{Ia}$ is degenerate with the IMF slope, motivating the uncertainties in its estimate.

If we multiply N_{Ia} by the IMF integral over the mass range of SN Ia progenitors, $\int_{3 M_\odot}^{8 M_\odot} \phi(m) dm \sim 0.016 M_\odot^{-1}$ (for our median $\log m_c$ and ξ), we obtain the number of SNe Ia produced per unit stellar mass with respect to the entire stellar population, i.e., dn_{Ia} / dM_\star . Using our N_{Ia} estimate, we obtain $dn_{Ia} / dM_\star = 5.6 \pm 1.4 \times 10^{-4} M_\odot^{-1}$. This is in accordance with previous works that computed this quantity using approaches similar to ours, where dn_{Ia} / dM_\star generally falls around $1 \times 10^{-3} M_\odot^{-1}$ [28,76,84,90–92,148]. The lower and higher values are, respectively, $3.4 \times 10^{-4} M_\odot^{-1}$ [76] and $1.14 \times 10^{-2} M_\odot^{-1}$ [91], accounting for uncertainties. The most distant results from $1 \times 10^{-3} M_\odot^{-1}$ are due to the adoption of extreme DTDs and SFRDs. In comparing our results with the literature, when needed, we convert their results to the quantity dn_{Ia} / dM_\star , accounting for the IMF adopted in each work.

f_{bin} is still quite uncertain (e.g., [149]). References [150,151] measure the local f_{bin} as a function of stellar mass via direct observations in the Solar neighborhood. According to their results, stars in the mass range of SN Ia progenitors (i.e., $3–8 M_\odot$, as assumed in

this work) would have a probability of between roughly 0.5 and 0.7 of lying in a binary (increasing with mass). Assuming that this measured f_{bin} behavior is valid also at higher redshifts, we fix f_{bin} and compute the quantity $b_{Ia} = N_{Ia}/f_{bin}$. b_{Ia} describes the fraction of stars in the mass range of SN Ia progenitors, which produce SNe Ia, given that they are in a binary system. If we fix $f_{bin} = 0.5$, we obtain $b_{Ia} = 7.0 \pm 1.8 \times 10^{-2}$. Fixing $f_{bin} = 0.7$ instead gives $b_{Ia} = 5.0 \pm 1.3 \times 10^{-2}$. This means that, accounting for the uncertainties in our N_{Ia} estimate and in f_{bin} , roughly from 4% to 10% of stars lying in binaries, with a mass in the SN Ia progenitor range, actually give rise to an SN Ia due to the processes happening in the binary.

As our results suggest, this kind of study offers the opportunity to constrain the properties of SN Ia progenitors and delve into aspects such as the relative contribution to the SN Ia rate coming from the SD and DD scenarios (see also, e.g., [93]) and the evolution of WD binary systems.

The upper mass limit of CCSN progenitors, M_{CC}^{up} , is very uncertain. Indeed, it is still not clear what the transition mass is between type II and type Ib/c CCSN subtypes, and at what masses failed SNe start to take place. M_{CC}^{up} might lie between ~ 20 and 25 M_\odot all the way up to 100 M_\odot . Our results point to $M_{CC}^{up} \in [35-95] \text{ M}_\odot$, with a median value of $\sim 58 \text{ M}_\odot$. Even though the observational constraints we employ do not allow us to add much to what is already known, this shows the potential of this type of study for estimating this quantity, especially with the growth of observational data in the future (e.g., [152–156]). It is worth mentioning that the lack of CCSN observations from progenitors above $\sim 20-25 \text{ M}_\odot$ might be due to observational biases. In particular, CCSNe from more massive progenitors might be too dim to be detected (e.g., [37,40,41]). In this case, it would be more correct to consider our parameter M_{CC}^{up} as the maximum mass of CCSN progenitors that can be observed. A possible addition to this work would thus be to correct for this observational bias and find the maximum mass of all CCSN progenitors, detectable or undetectable.

4.3. Long Gamma-Ray Bursts and Cosmic Metallicity Evolution

We see that adding the LGRB rate, and prescribing a cosmic Z evolution recipe, allows us to put constraints on relevant quantities related to LGRB progenitors and the cosmic metallicity evolution. LGRBs are expected to arise only at metallicities lower than a certain value of Z_{max} . Remarkably, we are able to constrain this quantity to $Z_{max} = 1.8_{-0.8}^{+4.4} \times 10^{-3}$, or $12 + \log(\text{O/H}) = 7.83_{-0.24}^{+0.54}$. As explained in Section 2, we find an interplay between Z_{max} and the dispersion in the galaxy metallicity distribution, σ_Z , and we are able to constrain the latter to $\sigma_Z = 0.49_{-0.27}^{+0.17}$. Reference [142] finds a threshold value of $12 + \log(\text{O/H}) = 8.6$, or $Z_{max} \sim 1 \times 10^{-2}$, which is somewhat higher than our result. Also, LGRB host galaxy studies tend to show a preference for Z_{max} from $\sim 6 \times 10^{-3}$ up to Solar values $\sim 2 \times 10^{-2}$ (e.g., [157–161]). On the other hand, the values generally found by single stellar evolution simulations are more consistent with our results, $Z_{max} \sim 2-6 \times 10^{-3}$ (e.g., [45,135,162]). Accounting for the possible binary nature of LGRB progenitors in simulations might significantly change the latter results. For example, rotating stars in binaries can keep most of their initial surface velocity, or even increase it, and might thus give rise to LGRBs even at higher metallicities (see, e.g., [161] and references therein). Moreover, the observed LGRB dependence on metallicity might also be due to an underlying IMF variability, rather than simply the progenitor evolution (e.g., [145,161]).

Similarly, as discussed for the SN Ia rate, we account for all uncertainties regarding LGRB progenitors and emission by putting a constant factor N_{LGRB} in front of the integral in Equation (14). In this way, we agnostically account for all conditions related to the progenitor rotation, the mass of the accretion disk that forms after the progenitor explodes as an SN, the nature of the remnant, the launch of the relativistic jet, and, finally, the conversion of its energy into LGRB emission. Moreover, we account for the possible binary nature of the progenitor, which might favor LGRB emission. We find $N_{LGRB} = 10_{-7}^{+23} \times 10^{-2}$, meaning that, as a median value, $\sim 10\%$ of stars in the mass range of LGRB progenitors satisfy the conditions for LGRB emission. Within a 1σ confidence level, this percentage ranges from

$\sim 3\%$ to $\sim 33\%$. As one can see from Figure 4, the uncertainties in this quantity are mostly due to those in the LGRB progenitor mass range. Indeed, despite the MCMC being able to retrieve a fit for M_{LGRB}^{low} and M_{LGRB}^{up} , the uncertainties are significant: $M_{LGRB}^{low} < 24 M_{\odot}$ and $M_{LGRB}^{up} > 51 M_{\odot}$ at 1σ . Given the huge uncertainty in these quantities in the literature, these results still give us an indication of where LGRB progenitor masses might lie.

There have been a number of associations of LGRBs with type Ib/c SNe, suggesting a common progenitor. SN Ib/c, or “stripped-envelope” supernovae, are a subtype of CCSNe arising from “Wolf-Rayet” stars that lost their envelope. As already presented, we find a maximum mass of CCSN progenitors, comprising both type II and Ib/c SNe, of $\sim 58^{+37}_{-23} M_{\odot}$ at 1σ . On the other hand, we obtain estimates of $M_{LGRB}^{low} < 24 M_{\odot}$ and $M_{LGRB}^{up} > 51 M_{\odot}$. Given the overlap of the mass ranges of CCSN and LGRB progenitors, and, in particular, between M_{CC}^{up} and M_{LGRB}^{up} , our results appear to be compatible with LGRB and SN Ib/c sharing a common progenitor, even though the uncertainties we find do not allow us to make any further statement. Nonetheless, this treatment suggests the potential of this type of study to unveil the nature of transient progenitors, any possible association among them, and other uncertain aspects such as failed SNe.

Finally, one of the open questions about LGRB progenitors revolves around the nature of the remnant, which is believed to be either a BH or an NS. According to the “collapsar” scenario, a highly spinning BH remnant surrounded by a sufficiently massive accretion disk would be a necessary condition to launch a relativistic jet. On the other hand, the “magnetar” scenario predicts the remnant to be a highly magnetized, and rapidly spinning, NS. In principle, one could use the results obtained in this work to distinguish between these two scenarios based on the constraints on the LGRB progenitor masses. For example, if M_{LGRB}^{low} was lying above the expected masses of the NS progenitors, then the “magnetar” hypothesis would be excluded in favour of the BH remnant one. However, the high uncertainties we obtain for these quantities prevent us from saying anything about this matter. It would be nonetheless intriguing to explore this aspect once more constraining data are available in the future (e.g., [145,163,164]).

4.4. Variation on the Cosmic Z Evolution Prescription

As explained above, in order to compute the LGRB rate as a function of redshift, we adopt the FMR by [136], further implementing the offset from the FMR found in [137]. In this section, we compare our results to the case where we do not consider the offset from [137] and only adopt the original [136] FMR (Figure 8). To ease the reading, we will refer to the two cases as C20 and C20+23. As one can see in Table A3 in Appendix D, the parameter estimates obtained in the C20 case are compatible with those obtained in this work (compare with Table 1).

As shown in Figure 8a,b, the galaxy metallicity decreases much more slowly with redshift for the C20 FMR with respect to the C20+23 one. By looking at Figure 8c,d, we can see that both FMRs seem to produce relatively good fits to the observational points. If we compute the corresponding chi squares, we actually find that the C20 case is somewhat disfavored, with $\chi^2_{LGRB} = 3.5$ as opposed to $\chi^2_{LGRB} = 1.5$ for the C20+23 FMR. This can be better appreciated by looking at Figure 8e,f, where we show the LGRB fit as a function of cosmic age instead of redshift. Indeed, the fit somehow struggles to intercept some of the points in the C20 case (Figure 8f). Even though the uncertainties and low significance of these results prevent us from drawing any robust conclusion, they might suggest the potential of this approach to discriminate between different Z evolutions in the future, with more LGRB observations available at high redshift. For example, if the results shown in this section were reproduced at higher significance level, then FMRs with a steeper decrease with redshift would be favored with respect to more constant ones.

5. Conclusions

In this work, we seek to find a new determination of the stellar IMF, inferred from the observed rates of stellar transients. We adopt a parametric approach in order to model the UV luminosity density, local SMD, and SN Ia, CCSN, and LGRB rates as a function of redshift, and constrain the model parameters in order to reproduce the observational data available for these quantities. Remarkably, we obtain an IMF compatible with those typically assumed based on stellar observations in the local Universe, e.g., the Salpeter, Kroupa, and Chabrier IMFs. In particular, we infer an IMF slope of $\xi = -2.53^{+0.24}_{-0.27}$, consistent with the usual values of -2.3 (Chabrier, Kroupa), -2.35 (Salpeter), and -2.7 (Kroupa, Scalo). We stress that our determination is completely independent from all previous ones. Moreover, our parametric approach allows us to keep the number of physical assumptions at the minimum, leading to a fully observation-driven IMF determination. We also find that, according to our results, a fraction $N_{Ia} = 3.5 \pm 0.9 \times 10^{-2}$ of stars in the mass range of SN Ia progenitors actually explode as SNe Ia due to the processes happening in the binaries.

The LGRB rate is not crucial for inferring the IMF, which can be robustly determined even by considering only the UV luminosity density, local SMD, and SN Ia and CCSN rates. However, considering the LGRB rate, along with an up-to-date, semi-empirical determination of the galaxy metallicity evolution throughout cosmic history, enables us to extend the study to LGRB progenitors and the cosmic metallicity evolution. Interestingly, an interplay emerges between the maximum metallicity of LGRB progenitors and the dispersion in the galaxy metallicity distribution. We find an estimate of $Z_{max} = 0.12^{+0.29}_{-0.05} M_{\odot}$, which is in accordance with previous theoretical determinations in the literature. Moreover, we find that a fraction $N_{LGRB} = 10^{+23}_{-7} \times 10^{-2}$ of stars in the mass range of LGRB progenitors actually produce an LGRB. This fraction agnostically accounts for all conditions required to have LGRB emission, including progenitor rotation, accretion disk mass, remnant nature, and jet-launching and jet-energy conversion to LGRB. Moreover, it might contain the possible effect of LGRBs arising in binary systems.

Finally, we attempt to constrain the masses of CCSN and LGRB progenitors. Due to the simplicity of the model, and the limits of the adopted constraints, we are only able to obtain $M_{CC}^{up} \sim 58^{+37}_{-23} M_{\odot}$ for the upper mass limit of CCSN progenitors. Similarly, we obtain $M_{LGRB}^{low} < 24 M_{\odot}$ and $M_{LGRB}^{up} > 51 M_{\odot}$ for LGRB progenitors. We also test the hypothesis of an IMF varying with redshift, finding no evidence of evolution for the IMF slope, while the characteristic mass exhibits a mild increase with redshift. Despite the uncertainties associated with these results, they show the potential of this approach to study the progenitors of stellar transients and their IMF, especially considering the increased wealth of data in the future. Indeed, a number of missions relevant to this purpose are programmed or already ongoing, such as the *Euclid*, *JWST*, the *Vera Rubin Observatory*, the *Nancy Grace Roman Space Telescope*, the *Zwicky Transient Facility*, *WFIRST*, *ULTIMATE-Subaru*, and the *Gamow Explorer* missions (e.g., [145,152–156,163–173]). In particular, up to thousands or even tens of thousands SNe are expected to be observed, reaching out to higher redshifts than are currently set (e.g., [152–156,166,170]). Moreover, new determinations of the SFRD and/or UV luminosity density are promised, especially at high redshifts, e.g., by the *JWST* (<https://www.stsci.edu/jwst/>). These achievements might also allow us to shed light on topics such as the competing scenarios for LGRB progenitors, their putative association with those of SNe Ib/c, and the IMF universality.

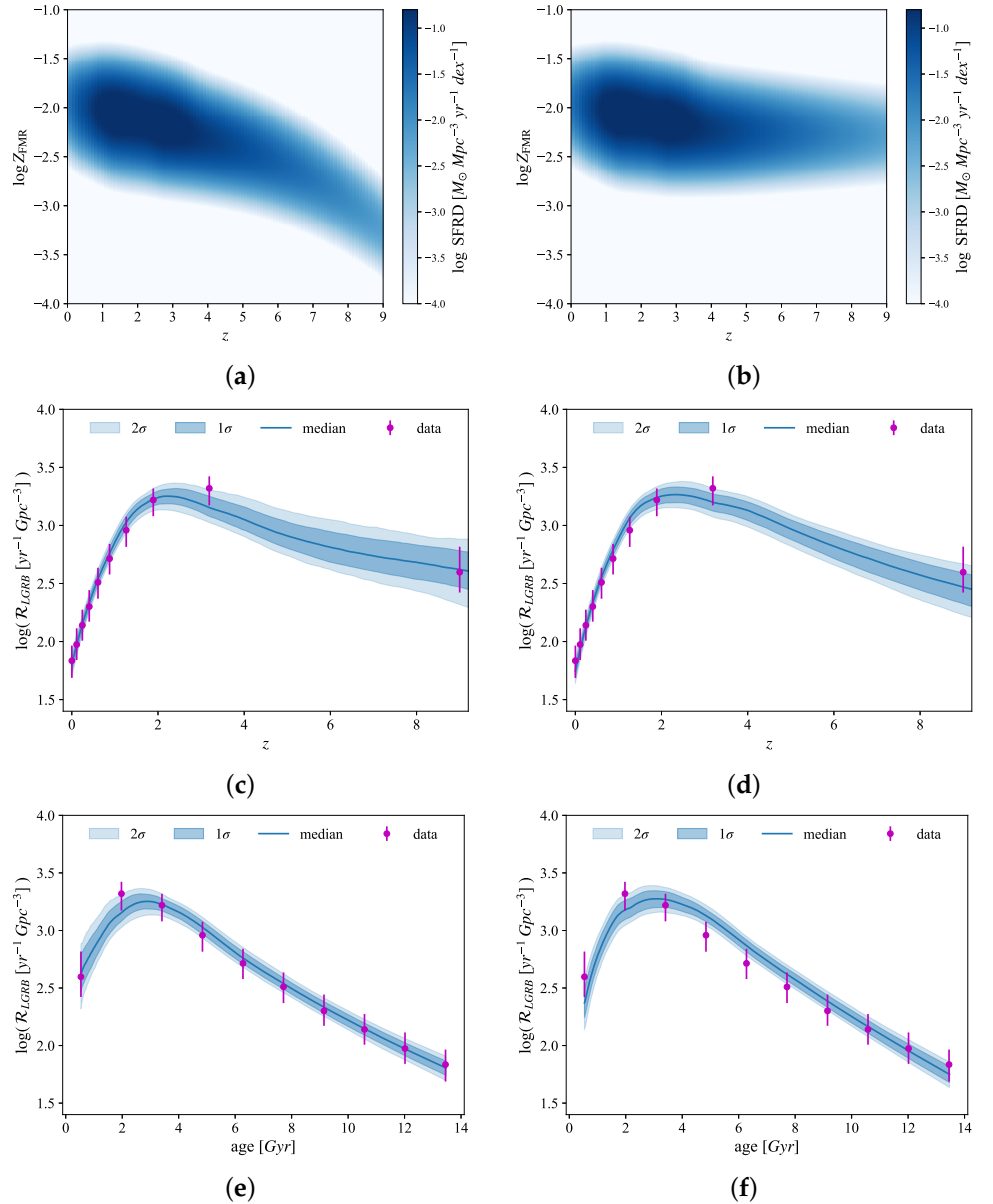


Figure 8. Comparison between the Z-dependent SFRDs (upper panels) and LGRB rate fits we obtain by adopting the FMR by [136] plus the offset from [137] (left panels) and the original FMR by [136] without the offset from [137] (right panels). We show the LGRB fits both as function of redshift (middle panels) and cosmic age (lower panels). σ_Z is fixed to 0.15 in the upper panels.

Author Contributions: Conceptualization: F.G., L.B. and A.L.; methodology: F.G., L.B. and A.L.; validation: L.B., A.L., G.G., O.S.S., R.S. and M.S.; writing: F.G. All authors have read and agreed to the published version of the manuscript.

Funding: This work is partially funded by the following: “Data Science methods for MultiMessenger Astrophysics & Multi-Survey Cosmology” funded by the Italian Ministry of University and Research, Programmazione triennale 2021/2023 (DM n. 2503 dd. 9 December 2019), Programma Congiunto Scuole; Italian Research Center on High Performance Computing Big Data and Quantum Computing (ICSC), project funded by European Union—NextGenerationEU—and National Recovery and Resilience Plan (NRRP)—Mission 4 Component 2 within the activities of Spoke 3 (Astrophysics and Cosmos Observations); PRIN MUR 2022 project no. 20224JR28W “Charting unexplored avenues in Dark Matter”; INAF Large Grant 2022 funding scheme with the project “MeerKAT and LOFAR Team up: a Unique Radio Window on Galaxy/AGN co-Evolution”; INAF GO-GTO Normal 2023

funding scheme with the project “Serendipitous H-ATLAS-fields Observations of Radio Extragalactic Sources (SHORES)”.

Data Availability Statement: The data presented in this study are available on request from the corresponding author.

Acknowledgments: We thank A. Bressan for insightful discussions concerning the exploitation of the PARSEC22 code, and P. Salucci for useful indications about galaxy stellar mass functions. We also thank T. Ronconi for precious advice on the implementation of the MCMC. Finally, we kindly thank F. Addari and C. Ugolini for useful conversations about type Ia and core-collapse supernovae.

Conflicts of Interest: The authors declare no conflicts of interest.

Appendix A. Update on LGRB Rate Determination by Ghirlanda and Salvaterra 2022

In this work, we consider the updated version of the LGRB rate determination as a function of redshift by [142]. This was obtained by updating the BAT6 sample used in [142], which contained 79 GRBs up to May 2014, with all the bursts that satisfy the definition of the BAT6 sample as described in [174]. This new sample contains 124 GRBs up to December 2022. With this new sample, the updated parameters (with their associated 1σ uncertainties) describing the LGRB rate as a function of redshift (see Equation (1) of [142]) are as follows: $\rho_0 = 68.33^{+23.87}_{-19.68} \text{ Gpc}^{-3} \text{ yr}^{-1}$, $p_{z,1} = 3.13^{+0.25}_{-0.28}$, $p_{z,2} = 3.44^{+0.21}_{-0.25}$, and $p_{z,3} = 5.33^{+0.37}_{-0.33}$, and the luminosity evolution parameter is $\delta = 1.05^{+0.38}_{-0.18}$. In Figure A1, we show a comparison between the two determinations. As one can see, the new LGRB rate peaks at slightly higher redshift, around $z \sim 3$, and decreases less steeply with respect to the old one, leading to an enhanced occurrence of LGRBs at high redshift.

Appendix B. Additional MCMC Results

We report in Figure A2 the corner plot containing the posterior probabilities we obtain for the whole parameter space regarding the IMF, $\rho_{UV}(z)$, $\rho_{\star,0}$, $R_{Ia}(z)$, $R_{CC}(z)$, $R_{LGRB}(z)$, and the cosmic Z evolution.

In Figure A3 and Table A1, we instead report the MCMC results obtained without considering LGRBs and the cosmic Z evolution, only employing the constraints on $\rho_{UV}(z)$, $\rho_{\star,0}$, $R_{Ia}(z)$, and $R_{CC}(z)$. As one can see, these results are compatible with those shown in Figure A2 (or Figure 2) and Table 1.

Table A1. Estimates of the model parameters for the case where we do not consider LGRBs and the cosmic Z evolution.

$\log \rho_{UV,0}$	$25.93^{+0.07}_{-0.08}$	$\log(\text{erg s}^{-1} \text{ Mpc}^{-3})$
α	$3.50^{+0.27}_{-0.31}$	-
β	6.32 ± 0.36	-
γ	$2.61^{+0.19}_{-0.23}$	-
$\log m_c$	$-0.95^{+0.39}_{-0.98}$	$\log(\text{M}_\odot)$
ξ	$-2.71^{+0.30}_{-0.33}$	-
$\log N_{Ia}$	$-1.54^{+0.11}_{-0.15}$	-
$\log M_{CC}^{up}$	1.73 ± 0.24	$\log(\text{M}_\odot)$
$\ln f$	$-4.32^{+0.21}_{-0.17}$	-

Appendix C. Additional Results for IMF Variation

In this section, we present the corner plot for the whole parameter space obtained in the case of the IMF being variable with redshift (Figure A4), as well as Table A2 with all parameter estimates, to supplement the results shown in Section 3.3.

Table A2. Estimates of the model parameters in the case of variable IMF with redshift.

$\log \rho_{UV,0}$	25.93 ± 0.07	$\log(\text{erg s}^{-1} \text{Mpc}^{-3})$
α	$3.11^{+0.22}_{-0.25}$	-
β	$6.31^{+0.38}_{-0.42}$	-
γ	$2.95^{+0.22}_{-0.26}$	-
$\log m_{c,0}$	-1.08 ± 0.51	$\log(\text{M}_\odot)$
ξ_0	$-2.55^{+0.25}_{-0.29}$	-
$\log N_{Ia}$	$-1.46^{+0.10}_{-0.11}$	-
$\log M_{CC}^{up}$	$1.79^{+0.38}_{-0.16}$	$\log(\text{M}_\odot)$
γ_{imf}	$0.53^{+0.21}_{-0.43}$	-
f_{imf}	< 0.026	-
z_0	—	-
σ_Z	$0.60^{+0.39}_{-0.12}$	-
$\log N_{LGRB}$	-1.15 ± 0.56	-
$\log Z_{max}$	$-2.44^{+0.56}_{-0.46}$	-
$\log M_{LGRB}^{low}$	< 1.45	$\log(\text{M}_\odot)$
$\log M_{LGRB}^{up}$	> 1.73	$\log(\text{M}_\odot)$
$\ln f$	$-4.38^{+0.26}_{-0.19}$	-

Appendix D. Parameter Estimates for the FMR Variation

We report in Table A3 the parameter estimates returned by the MCMC for the FMR variation by [136], without the offset from [137] that we instead implement in this work.

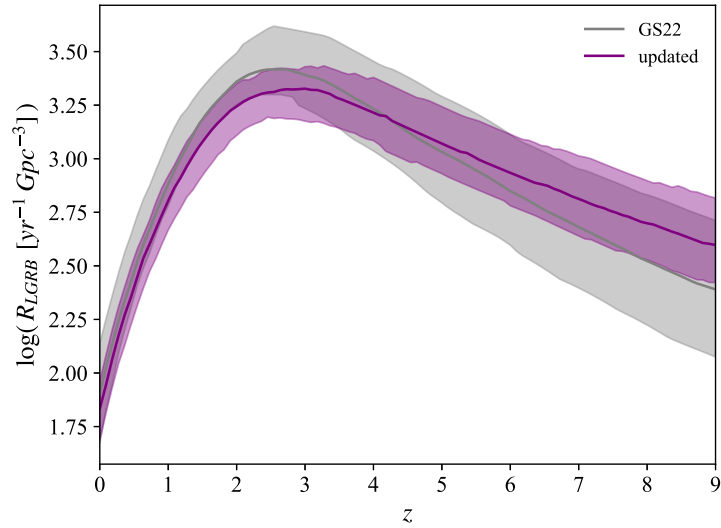


Figure A1. Comparison between the LGRB rate as a function of redshift obtained in [142] (gray line) and the updated determination employed in this work, accounting for more recent LGRB observations (purple line). Bands represent the corresponding 1σ uncertainties.

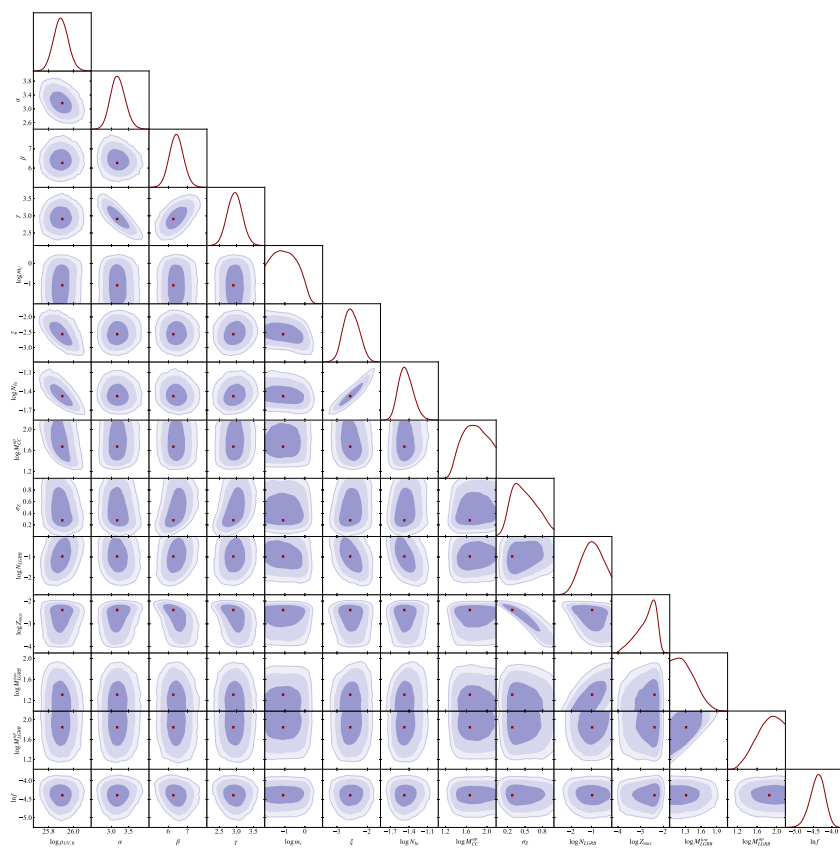


Figure A2. Same as Figure 2, for the whole parameter space.

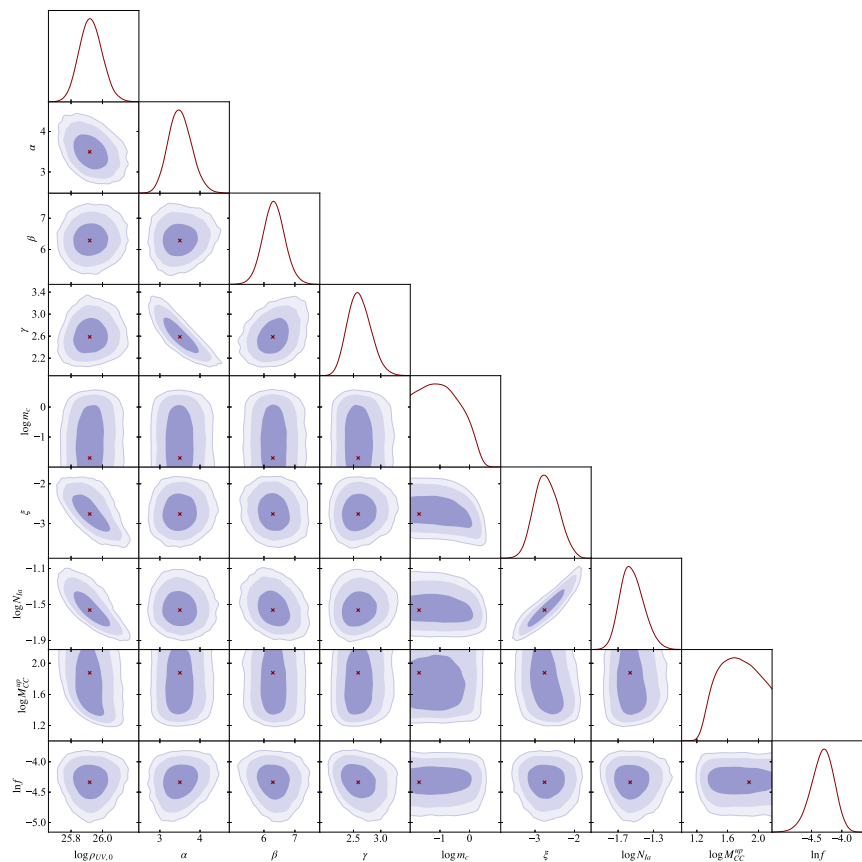


Figure A3. Same as Figure A2, for the case where we do not consider LGRBs and the cosmic Z evolution.

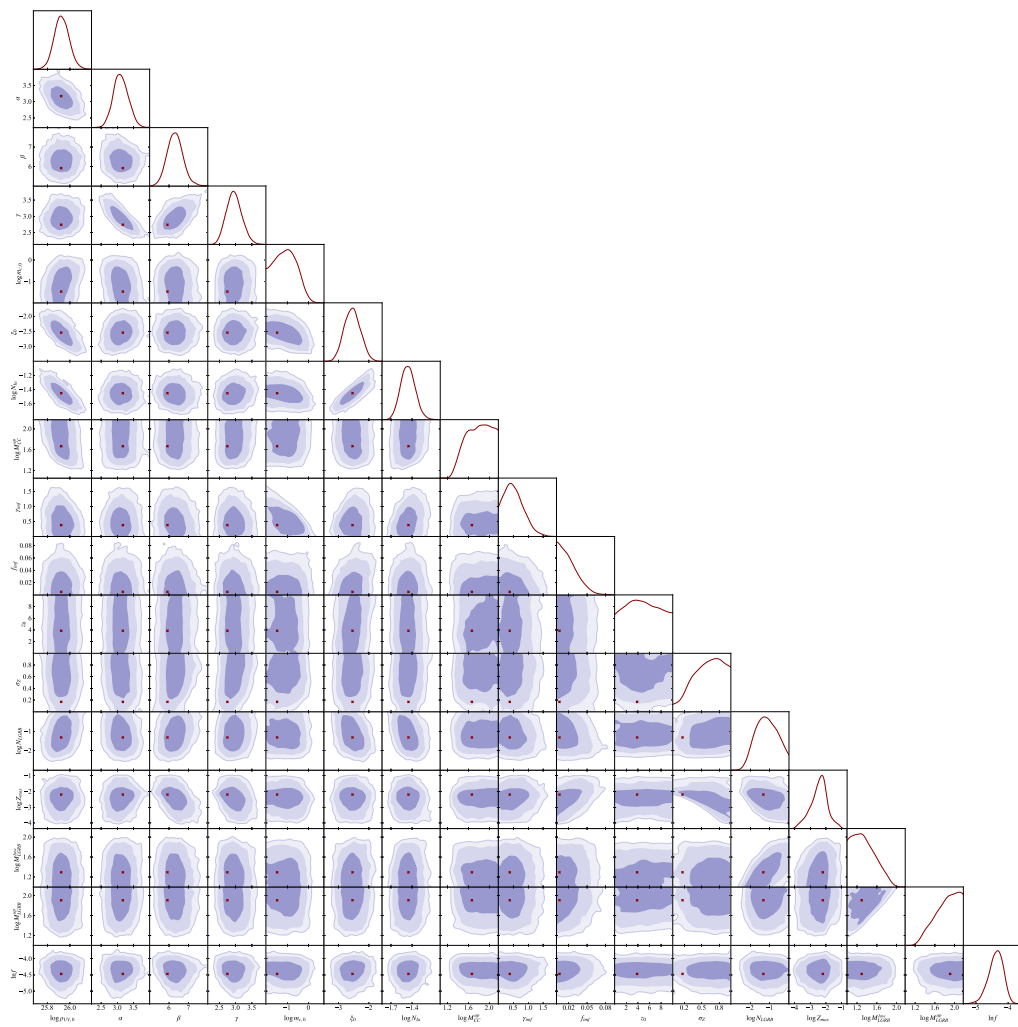


Figure A4. Corner plot with individual and joint posterior probabilities for the case of IMF variable with redshift, for the whole parameter space. For other details, see the caption of Figure 2.

Table A3. Parameter estimates for the variation with FMR by [136], without the offset from [137].

$\log \rho_{UV,0}$	$25.88^{+0.05}_{-0.06}$	$\log(\text{erg s}^{-1} \text{Mpc}^{-3})$
α	3.32 ± 0.23	-
β	5.93 ± 0.28	-
γ	2.74 ± 0.20	-
$\log m_c$	$-0.94^{+0.60}_{-0.74}$	$\log(\text{M}_\odot)$
ξ	-2.46 ± 0.25	-
$\log N_{Ia}$	$-1.41^{+0.11}_{-0.13}$	-
$\log M_{CC}^{up}$	1.76 ± 0.22	$\log(\text{M}_\odot)$
σ_Z	$0.36^{+0.11}_{-0.14}$	-
$\log N_{LGRB}$	$-0.69^{+0.68}_{-0.18}$	-
$\log Z_{max}$	$-2.76^{+0.46}_{-0.30}$	-
$\log M_{LGRB}^{low}$	< 1.34	$\log(\text{M}_\odot)$
$\log M_{LGRB}^{up}$	$1.82^{+0.33}_{-0.13}$	$\log(\text{M}_\odot)$
$\ln f$	$-4.32^{+0.19}_{-0.16}$	-

References

1. Hennebelle, P.; Grudic, M. The Physical Origin of the Stellar Initial Mass Function. *arXiv* **2024**, arXiv:2404.07301. [[CrossRef](#)]
2. Salpeter, E.E. The Luminosity Function and Stellar Evolution. *Astrophys. J.* **1955**, *121*, 161. [[CrossRef](#)]

3. Scalo, J.M. The Stellar Initial Mass Function. *FCPh* **1986**, *11*, 1–278.

4. Kroupa, P.; Tout, C.A.; Gilmore, G. The Distribution of Low-Mass Stars in the Galactic Disc. *Mon. Not. R. Astron. Soc.* **1993**, *262*, 545–587. [\[CrossRef\]](#)

5. Scalo, J.; Vázquez-Semadeni, E.; Chappell, D.; Passot, T. On the Probability Density Function of Galactic Gas. I. Numerical Simulations and the Significance of the Polytropic Index. *Astrophys. J.* **1998**, *504*, 835–853. [\[CrossRef\]](#)

6. Kroupa, P. On the variation of the initial mass function. *Mon. Not. R. Astron. Soc.* **2001**, *322*, 231–246. [\[CrossRef\]](#)

7. Chabrier, G. Galactic Stellar and Substellar Initial Mass Function. *PASP* **2003**, *115*, 763–795. [\[CrossRef\]](#)

8. Kroupa, P.; Weidner, C.; Pflamm-Altenburg, J.; Thies, I.; Dabringhausen, J.; Marks, M.; Maschberger, T. The Stellar and Sub-Stellar Initial Mass Function of Simple and Composite Populations. In *Planets, Stars and Stellar Systems. Volume 5: Galactic Structure and Stellar Populations*; Oswalt, T.D., Gilmore, G., Eds.; Springer: Dordrecht, The Netherlands, 2013; Volume 5, p. 115. [\[CrossRef\]](#)

9. Kroupa, P.; Jerabkova, T. *Star-Formation Rates of Galaxies*; Cambridge University Press: Cambridge, UK, 2021. [\[CrossRef\]](#)

10. Weisz, D.R.; Fouesneau, M.; Hogg, D.W.; Rix, H.W.; Dolphin, A.E.; Dalcanton, J.J.; Foreman-Mackey, D.T.; Lang, D.; Clifton Johnson, L.; Beerman, L.C.; et al. The Panchromatic Hubble Andromeda Treasury. IV. A Probabilistic Approach to Inferring the High-Mass Stellar Initial Mass Function and other Power-Law Functions. *Astrophys. J.* **2012**, *762*, 123. [\[CrossRef\]](#)

11. Wainer, T.M.; Williams, B.F.; Johnson, L.C.; Weisz, D.R.; Dalcanton, J.J.; Seth, A.C.; Dolphin, A.; Durbin, M.J.; Bell, E.F.; Chen, Z.; et al. The Panchromatic Hubble Andromeda Treasury: Triangulum Extended Region (PHATTER). VI. The High-Mass Stellar Initial Mass Function of M33. *arXiv* **2024**, arXiv:2406.12129. [\[CrossRef\]](#)

12. Strøgård, L.G.; Dahlen, T.; Rodney, S.A.; Graur, O.; Riess, A.G.; McCully, C.; Ravindranath, S.; Mobasher, B.; Shahady, A.K. The Rate of Core Collapse Supernovae to Redshift 2.5 from the Candels and Clash Supernova Surveys. *Astrophys. J.* **2015**, *813*, 93. [\[CrossRef\]](#)

13. Stanway, E.R.; Eldridge, J.J. Initial mass function variations cannot explain the ionizing spectrum of low metallicity starbursts. *Astron. Astrophys.* **2019**, *621*, A105. [\[CrossRef\]](#)

14. Ziegler, J.J.; Edwards, T.D.P.; Suliga, A.M.; Tamborra, I.; Horiuchi, S.; Ando, S.; Freese, K. Non-universal stellar initial mass functions: Large uncertainties in star formation rates at $z = 2\text{--}4$ and other astrophysical probes. *Mon. Not. R. Astron. Soc.* **2022**, *517*, 2471–2484. [\[CrossRef\]](#)

15. Li, J.; Liu, C.; Zhang, Z.Y.; Tian, H.; Fu, X.; Li, J.; Yan, Z.Q. Stellar initial mass function varies with metallicity and time. *Nature* **2023**, *613*, 460–462. [\[CrossRef\]](#)

16. Martín-Navarro, I.; de Lorenzo-Cáceres, A.; Gadotti, D.A.; Méndez-Abreu, J.; Falcón-Barroso, J.; Sánchez-Blázquez, P.; Coelho, P.; Neumann, J.; van de Ven, G.; Pérez, I. The universal variability of the stellar initial mass function probed by the TIMER survey. *arXiv* **2023**, arXiv:2312.13355. [\[CrossRef\]](#)

17. Maksymowicz-Maciata, M.; Spiniello, C.; Martín-Navarro, I.; Ferré-Mateu, A.; Bevacqua, D.; Cappellari, M.; D’Ago, G.; Tortora, C.; Arnaboldi, M.; Hartke, J.; et al. INSPIRE: INvestigating Stellar Population In RElics VI—The low-mass end slope of the stellar Initial Mass Function and chemical composition. *arXiv* **2024**, arXiv:2401.15769. [\[CrossRef\]](#)

18. Bouwens, R.J.; Oesch, P.A.; Stefanon, M.; Illingworth, G.; Labbe, I.; Reddy, N.; Atek, H.; Montes, M.; Naidu, R.; Nanayakkara, T.; et al. New Determinations of the UV Luminosity Functions from $z=9$ to 2 Show a Remarkable Consistency with Halo Growth and a Constant Star Formation Efficiency. *Astron. J.* **2021**, *162*, 47. [\[CrossRef\]](#)

19. Bouwens, R.; Illingworth, G.; Oesch, P.; Stefanon, M.; Naidu, R.; van Leeuwen, I.; Magee, D. UV luminosity density results at $z>8$ from the first JWST/NIRCam fields: Limitations of early data sets and the need for spectroscopy. *Mon. Not. R. Astron. Soc.* **2023**, *523*, 1009–1035. [\[CrossRef\]](#)

20. Donnan, C.T.; McLeod, D.J.; Dunlop, J.S.; McLure, R.J.; Carnall, A.C.; Begley, R.; Cullen, F.; Hamadouche, M.L.; Bowler, R.A.A.; Magee, D.; et al. The evolution of the galaxy UV luminosity function at redshifts $z = 8\text{--}15$ from deep JWST and ground-based near-infrared imaging. *Mon. Not. R. Astron. Soc.* **2022**, *518*, 6011–6040. [\[CrossRef\]](#)

21. Harikane, Y.; Ouchi, M.; Oguri, M.; Ono, Y.; Nakajima, K.; Isobe, Y.; Umeda, H.; Mawatari, K.; Zhang, Y. A Comprehensive Study of Galaxies at $z = 9\text{--}16$ Found in the Early JWST Data: Ultraviolet Luminosity Functions and Cosmic Star Formation History at the Pre-reionization Epoch. *Astrophys. J. Suppl. Ser.* **2023**, *265*, 5. [\[CrossRef\]](#)

22. Kennicutt, R.C.; Evans, N.J. Star Formation in the Milky Way and Nearby Galaxies. *Annu. Rev. Astron. Astrophys.* **2012**, *50*, 531–608. [\[CrossRef\]](#)

23. Foreman-Mackey, D.; Hogg, D.W.; Lang, D.; Goodman, J. emcee: The MCMC Hammer. *Publ. Astron. Soc. Pac.* **2013**, *125*, 306–312. [\[CrossRef\]](#)

24. Madau, P.; Dickinson, M. Cosmic Star-Formation History. *Annu. Rev. Astron. Astrophys.* **2014**, *52*, 415–486. [\[CrossRef\]](#)

25. Cai, Z.Y.; Lapi, A.; Bressan, A.; De Zotti, G.; Negrello, M.; Danese, L. A Physical Model for the Evolving Ultraviolet Luminosity Function of High Redshift Galaxies and their Contribution to the Cosmic Reionization. *Astrophys. J.* **2014**, *785*, 65. [\[CrossRef\]](#)

26. Robertson, B.E.; Ellis, R.S.; Furlanetto, S.R.; Dunlop, J.S. Cosmic Reionization and Early Star-Forming Galaxies: A Joint Analysis of New Constraints from Planck and the Hubble Space Telescope. *Astrophys. J.* **2015**, *802*, L19. [\[CrossRef\]](#)

27. Finkelstein, S.L.; D’Aloisio, A.; Paardekooper, J.P.; Jr., R.R.; Behroozi, P.; Finlator, K.; Livermore, R.; Sanderbeck, P.R.U.; Vecchia, C.D.; Khochfar, S. Conditions for Reionizing the Universe with a Low Galaxy Ionizing Photon Escape Fraction. *Astrophys. J.* **2019**, *879*, 36. [\[CrossRef\]](#)

28. Madau, P.; Della Valle, M.; Panagia, N. On the evolution of the cosmic supernova rates. *Mon. Not. R. Astron. Soc.* **1998**, *297*, L17–L22. [\[CrossRef\]](#)

29. Maoz, D.; Mannucci, F.; Nelemans, G. Observational Clues to the Progenitors of Type Ia Supernovae. *Annu. Rev. Astron. Astrophys.* **2014**, *52*, 107–170. [\[CrossRef\]](#)

30. Bethe, H.A.; Wilson, J.R. Revival of a stalled supernova shock by neutrino heating. *Astrophys. J.* **1985**, *295*, 14–23. [\[CrossRef\]](#)

31. Burrows, A.; Hayes, J.; Fryxell, B.A. On the Nature of Core-Collapse Supernova Explosions. *Astrophys. J.* **1995**, *450*, 830. [\[CrossRef\]](#)

32. Janka, H.T.; Müller, E. Neutrino heating, convection, and the mechanism of Type-II supernova explosions. *Astron. Astrophys.* **1996**, *306*, 167.

33. Burrows, A.; Radice, D.; Vartanyan, D. Three-dimensional supernova explosion simulations of 9-, 10-, 11-, 12-, and 13- M_{\odot} stars. *Mon. Not. R. Astron. Soc.* **2019**, *485*, 3153–3168. [\[CrossRef\]](#)

34. Aguilera-Dena, D.R.; Müller, B.; Antoniadis, J.; Langer, N.; Dessart, L.; Vigna-Gómez, A.; Yoon, S.C. Stripped-envelope stars in different metallicity environments: II. Type I supernovae and compact remnants. *Astron. Astrophys.* **2023**, *671*, A134. [\[CrossRef\]](#)

35. Heger, A.; Woosley, S.E. The Nucleosynthetic Signature of Population III. *Astrophys. J.* **2002**, *567*, 532. [\[CrossRef\]](#)

36. Heger, A.; Fryer, C.L.; Woosley, S.E.; Langer, N.; Hartmann, D.H. How Massive Single Stars End Their Life. *Astrophys. J.* **2003**, *591*, 288. [\[CrossRef\]](#)

37. Smartt, S.J. Observational Constraints on the Progenitors of Core-Collapse Supernovae: The Case for Missing High-Mass Stars. *Publ. Astron. Soc. Aust.* **2015**, *32*, e016. [\[CrossRef\]](#)

38. Timmes, F.X.; Woosley, S.E.; Weaver, T.A. The Neutron Star and Black Hole Initial Mass Function. *Astrophys. J.* **1996**, *457*, 834. [\[CrossRef\]](#)

39. Zhang, W.; Woosley, S.E.; Heger, A.Fallback and Black Hole Production in Massive Stars. *Astrophys. J.* **2008**, *679*, 639. [\[CrossRef\]](#)

40. Coughlin, E.R.; Quataert, E.; Fernández, R.; Kasen, D. A physical model of mass ejection in failed supernovae. *Mon. Not. R. Astron. Soc.* **2018**, *477*, 1225–1238. [\[CrossRef\]](#)

41. Antoni, A.; Quataert, E. Numerical simulations of the random angular momentum in convection—II. Delayed explosions of red supergiants following ‘failed’ supernovae. *Mon. Not. R. Astron. Soc.* **2023**, *525*, 1229–1245. [\[CrossRef\]](#)

42. Mészáros, P. Gamma-ray bursts. *Rep. Prog. Phys.* **2006**, *69*, 2259–2321. [\[CrossRef\]](#)

43. Iwamoto, K.; Mazzali, P.; Nomoto, K.; Umeda, H.; Nakamura, T.; Patat, F.; Danziger, I.; Young, T.; Suzuki, T.; Shigeyama, T.; et al. A hypernova model for the supernova associated with the γ -ray burst of 25 April 1998. *Nature* **1998**, *395*, 672–674. [\[CrossRef\]](#)

44. Nomoto, K.; Maeda, K.; Tominaga, N.; Ohkubo, T.; Umeda, H.; Deng, J.; Mazzali, P. Hypernovae: Their Properties and Gamma-Ray Burst Connection. *Prog. Theor. Phys. Suppl.* **2004**, *155*, 299–302. [\[CrossRef\]](#)

45. Woosley, S.; Bloom, J. The Supernova Gamma-Ray Burst Connection. *Annu. Rev. Astron. Astrophys.* **2006**, *44*, 507–556. [\[CrossRef\]](#)

46. Mazzali, P.A.; Deng, J.; Nomoto, K.; Sauer, D.N.; Pian, E.; Tominaga, N.; Tanaka, M.; Maeda, K.; Filippenko, A.V. A neutron-star-driven X-ray flash associated with supernova SN 2006aj. *Nature* **2006**, *442*, 1018–1020. [\[CrossRef\]](#) [\[PubMed\]](#)

47. Mazzali, P.A.; Valenti, S.; Della Valle, M.; Chincarini, G.; Sauer, D.N.; Benetti, S.; Pian, E.; Piran, T.; D’Elia, V.; Elias-Rosa, N.; et al. The Metamorphosis of Supernova SN 2008D/XRF 080109: A Link Between Supernovae and GRBs/Hypernovae. *Science* **2008**, *321*, 1185. [\[CrossRef\]](#)

48. Valenti, S.; Benetti, S.; Cappellaro, E.; Patat, F.; Mazzali, P.; Turatto, M.; Hurley, K.; Maeda, K.; Gal-Yam, A.; Foley, R.; et al. The broad-lined Type Ic supernova 2003jd. *Mon. Not. R. Astron. Soc.* **2008**, *383*, 1485–1500. [\[CrossRef\]](#)

49. Hjorth, J.; Bloom, J.S. The Gamma-Ray Burst—Supernova Connection. *arXiv* **2011**, arXiv:1104.2274. [\[CrossRef\]](#)

50. Caffau, E.; Ludwig, H.G.; Steffen, M.; Freytag, B.; Bonifacio, P. Solar Chemical Abundances Determined with a CO 5BOLD 3D Model Atmosphere. *Sol. Phys.* **2010**, *268*, 255–269. [\[CrossRef\]](#)

51. Larson, R.B. Early star formation and the evolution of the stellar initial mass function in galaxies. *Mon. Not. R. Astron. Soc.* **1998**, *301*, 569–581. [\[CrossRef\]](#)

52. Bressan, A.; Marigo, P.; Girardi, L.; Salasnich, B.; Cero, C.D.; Rubele, S.; Nanni, A. Stellar tracks and isochrones with the PAdova and TRIeste Stellar Evolution Code. *Mon. Not. R. Astron. Soc.* **2012**, *427*, 127–145. [\[CrossRef\]](#)

53. Chen, Y.; Girardi, L.; Bressan, A.; Marigo, P.; Barbieri, M.; Kong, X. Improving PARSEC models for very low mass stars. *Mon. Not. R. Astron. Soc.* **2014**, *444*, 2525–2543. [\[CrossRef\]](#)

54. Chen, Y.; Bressan, A.; Girardi, L.; Marigo, P.; Kong, X.; Lanza, A. parsec evolutionary tracks of massive stars up to 350 at metallicities 0.0001 Z 0.04. *Mon. Not. R. Astron. Soc.* **2015**, *452*, 1068–1080. [\[CrossRef\]](#)

55. Tang, J.; Bressan, A.; Rosenfield, P.; Slemer, A.; Marigo, P.; Girardi, L.; Bianchi, L. New PARSEC evolutionary tracks of massive stars at low metallicity: testing canonical stellar evolution in nearby star-forming dwarf galaxies. *Mon. Not. R. Astron. Soc.* **2014**, *445*, 4287–4305. [\[CrossRef\]](#)

56. Costa, G.; Girardi, L.; Bressan, A.; Marigo, P.; Rodrigues, T.S.; Chen, Y.; Lanza, A.; Goudfrooij, P. Mixing by overshooting and rotation in intermediate-mass stars. *Mon. Not. R. Astron. Soc.* **2019**, *485*, 4641–4657. [\[CrossRef\]](#)

57. Costa, G.; Bressan, A.; Mapelli, M.; Marigo, P.; Iorio, G.; Spera, M. Formation of GW190521 from stellar evolution: The impact of the hydrogen-rich envelope, dredge-up, and $^{12}\text{C}(\text{a},\text{g})^{16}\text{O}$ rate on the pair-instability black hole mass gap. *Mon. Not. R. Astron. Soc.* **2020**, *501*, 4514–4533. [\[CrossRef\]](#)

58. Nguyen, C.T.; Costa, G.; Girardi, L.; Volpato, G.; Bressan, A.; Chen, Y.; Marigo, P.; Fu, X.; Goudfrooij, P. PARSEC V2.0: Stellar tracks and isochrones of low- and intermediate-mass stars with rotation. *Astron. Astrophys.* **2022**, *665*, A126. [\[CrossRef\]](#)

59. Goswami, S.; Slemer, A.; Marigo, P.; Bressan, A.; Silva, L.; Spera, M.; Boco, L.; Grisoni, V.; Pantoni, L.; Lapi, A. The effects of the initial mass function on Galactic chemical enrichment. *Astron. Astrophys.* **2021**, *650*, A203. [\[CrossRef\]](#)

60. Goswami, S.; Silva, L.; Bressan, A.; Grisoni, V.; Costa, G.; Marigo, P.; Granato, G.L.; Lapi, A.; Spera, M. Impact of very massive stars on the chemical evolution of extremely metal-poor galaxies. *Astron. Astrophys.* **2022**, *663*, A1. [\[CrossRef\]](#)

61. Gruppioni, C.; Pozzi, F.; Rodighiero, G.; Delvecchio, I.; Berta, S.; Pozzetti, L.; Zamorani, G.; Andreani, P.; Cimatti, A.; Ilbert, O.; et al. The Herschel PEP/HerMES luminosity function—I. Probing the evolution of PACS selected Galaxies to $z=4$. *Mon. Not. R. Astron. Soc.* **2013**, *432*, 23–52. [\[CrossRef\]](#)

62. Rowan-Robinson, M.; Oliver, S.; Wang, L.; Farrah, D.; Clements, D.L.; Gruppioni, C.; Marchetti, L.; Rigopoulou, D.; Vaccari, M. The star formation rate density from $z = 1$ to 6. *Mon. Not. R. Astron. Soc.* **2016**, *461*, 1100–1111. [\[CrossRef\]](#)

63. Dunlop, J.S.; McLure, R.J.; Biggs, A.D.; Geach, J.E.; Michałowski, M.J.; Ivison, R.J.; Rujopakarn, W.; van Kampen, E.; Kirkpatrick, A.; Pope, A.; et al. A deep ALMA image of the Hubble Ultra Deep Field. *Mon. Not. R. Astron. Soc.* **2016**, *466*, 861–883. [\[CrossRef\]](#)

64. Novak, M.; Smolčić, V.; Delhaize, J.; Delvecchio, I.; Zamorani, G.; Baran, N.; Bondi, M.; Capak, P.; Carilli, C.L.; Ciliegi, P.; et al. The VLA-COSMOS 3 GHz Large Project: Cosmic star formation history since $z=5$. *Astron. Astrophys.* **2017**, *602*, A5. [\[CrossRef\]](#)

65. Liu, D.; Daddi, E.; Dickinson, M.; Owen, F.; Pannella, M.; Sargent, M.; Béthermin, M.; Magdis, G.; Gao, Y.; Shu, X.; et al. “Super-deblended” Dust Emission in Galaxies. I. The GOODS-North Catalog and the Cosmic Star Formation Rate Density out to Redshift 6. *Astrophys. J.* **2018**, *853*, 172. [\[CrossRef\]](#)

66. Oesch, P.A.; Bouwens, R.J.; Illingworth, G.D.; LabbE, I.; Stefanon, M. The Dearth of $z=10$ Galaxies in All HST Legacy Fields—The Rapid Evolution of the Galaxy Population in the First 500 Myr. *Astrophys. J.* **2018**, *855*, 105. [\[CrossRef\]](#)

67. Bhatawdekar, R.; Conselice, C.J.; Margalef-Bentabol, B.; Duncan, K. Evolution of the galaxy stellar mass functions and UV luminosity functions at $z=6$ –9 in the Hubble Frontier Fields. *Mon. Not. R. Astron. Soc.* **2019**, *486*, 3805–3830. [\[CrossRef\]](#)

68. Gruppioni, C.; BEthermin, M.; Loiacono, F.; Le Fèvre, O.; Capak, P.; Cassata, P.; Faisst, A.L.; Schaefer, D.; Silverman, J.; Yan, L.; et al. The ALPINE-ALMA [CII] survey: The nature, luminosity function, and star formation history of dusty galaxies up to $z=6$. *Astron. Astrophys.* **2020**, *643*, A8. [\[CrossRef\]](#)

69. Spera, M.; Mapelli, M. Very massive stars, pair-instability supernovae and intermediate-mass black holes with the sevn code. *Mon. Not. R. Astron. Soc.* **2017**, *470*, 4739–4749. [\[CrossRef\]](#)

70. Cummings, J.D.; Kalirai, J.S.; Tremblay, P.E.; Ramirez-Ruiz, E.; Choi, J. The White Dwarf Initial–Final Mass Relation for Progenitor Stars from 0.85 to 7.5 Msun. *Astrophys. J.* **2018**, *866*, 21. [\[CrossRef\]](#)

71. Marigo, P.; Cummings, J.D.; Curtis, J.L.; Kalirai, J.; Chen, Y.; Tremblay, P.E.; Ramirez-Ruiz, E.; Bergeron, P.; Bladh, S.; Bressan, A.; et al. Carbon star formation as seen through the non-monotonic initial–final mass relation. *Nat. Astron.* **2020**, *4*, 1102–1110. [\[CrossRef\]](#)

72. Marigo, P. The Initial-Final Mass Relation of White Dwarfs: A Tool to Calibrate the Third Dredge-up. *arXiv* **2022**, arXiv:2204.06470. [\[CrossRef\]](#)

73. Weaver, J.R.; Davidzon, I.; Toft, S.; Ilbert, O.; McCracken, H.J.; Gould, K.M.L.; Jespersen, C.K.; Steinhardt, C.; Lagos, C.D.P.; Capak, P.L.; et al. COSMOS2020: The galaxy stellar mass function: The assembly and star formation cessation of galaxies at $0.2 < z \leq 7.5$. *Astron. Astrophys.* **2023**, *677*, A184. [\[CrossRef\]](#)

74. Cappellaro, E.; Evans, R.; Turatto, M. A new determination of supernova rates and a comparison with indicators for galactic star formation. *Astron. Astrophys.* **1999**, *351*, 459.

75. Cappellaro, E.; Riello, M.; Altavilla, G.; Botticella, M.T.; Benetti, S.; Clocchiatti, A.; Danziger, J.I.; Mazzali, P.; Pastorello, A.; Patat, F.; et al. Death rate of massive stars at redshift ~ 0.3 . *Astron. Astrophys.* **2005**, *430*, 83–93. [\[CrossRef\]](#)

76. Botticella, M.T.; Riello, M.; Cappellaro, E.; Benetti, S.; Altavilla, G.; Pastorello, A.; Turatto, M.; Greggio, L.; Patat, F.; Valenti, S.; et al. Supernova rates from the Southern inTermediate Redshift ESO Supernova Search (STRESS). *Astron. Astrophys.* **2007**, *479*, 49–66. [\[CrossRef\]](#)

77. Bazin, G.; Palanque-Delabrouille, N.; Rich, J.; Ruhlmann-Kleider, V.; Aubourg, E.; Le Guillou, L.; Astier, P.; Balland, C.; Basa, S.; Carlberg, R.G.; et al. The core-collapse rate from the Supernova Legacy Survey. *Astron. Astrophys.* **2009**, *499*, 653–660. [\[CrossRef\]](#)

78. Graur, O.; Poznanski, D.; Maoz, D.; Yasuda, N.; Totani, T.; Fukugita, M.; Filippenko, A.V.; Foley, R.J.; Silverman, J.M.; Gal-Yam, A.; et al. Supernovae in the Subaru Deep Field: The rate and delay-time distribution of Type Ia supernovae out to redshift 2: Supernovae in the Subaru Deep Field. *Mon. Not. R. Astron. Soc.* **2011**, *417*, 916–940. [\[CrossRef\]](#)

79. Li, W.; Chornock, R.; Leaman, J.; Filippenko, A.V.; Poznanski, D.; Wang, X.; Ganeshalingam, M.; Mannucci, F. Nearby supernova rates from the Lick Observatory Supernova Search—III. The rate-size relation, and the rates as a function of galaxy Hubble type and colour. *Mon. Not. R. Astron. Soc.* **2011**, *412*, 1473–1507. [\[CrossRef\]](#)

80. Dahlen, T.; Strolger, L.G.; Riess, A.G.; Mattila, S.; Kankare, E.; Mobasher, B. The Extended Hubble Space Telescope Supernova Survey: The Rate of Core Collapse Supernovae to $z = 1$. *Astrophys. J.* **2012**, *757*, 70. [\[CrossRef\]](#)

81. Mattila, S.; Dahlen, T.; Efstathiou, A.; Kankare, E.; Melinder, J.; Alonso-Herrero, A.; PErez-Torres, M.A.; Ryder, S.; Väisänen, P.; Östlin, G. Core-Collapse Supernovae Missed by Optical Surveys. *Astrophys. J.* **2012**, *756*, 111. [\[CrossRef\]](#)

82. Melinder, J.; Dahlen, T.; Mencía Trinchant, L.; Östlin, G.; Mattila, S.; Sollerman, J.; Fransson, C.; Hayes, M.; Kankare, E.; Nasoudi-Shoar, S. The rate of supernovae at redshift 0.1–1.0: The Stockholm VIMOS Supernova Survey III. *Astron. Astrophys.* **2012**, *545*, A96. [\[CrossRef\]](#)

83. Taylor, M.; Cinabro, D.; Dilday, B.; Galbany, L.; Gupta, R.R.; Kessler, R.; Marriner, J.; Nichol, R.C.; Richmond, M.; Schneider, D.P.; et al. The Core Collapse Supernova Rate from the SDSS-II Supernova Survey. *Astrophys. J.* **2014**, *792*, 135. [\[CrossRef\]](#)

84. Cappellaro, E.; Botticella, M.T.; Pignata, G.; Grado, A.; Greggio, L.; Limatola, L.; Vaccari, M.; Baruffolo, A.; Benetti, S.; Bufano, F.; et al. Supernova rates from the SUDARE VST-OmegaCAM search: I. Rates per unit volume. *Astron. Astrophys.* **2015**, *584*, A62. [\[CrossRef\]](#)

85. Graur, O.; Bianco, F.B.; Modjaz, M. A unified explanation for the supernova rate-galaxy mass dependence based on supernovae detected in Sloan galaxy spectra. *Mon. Not. R. Astron. Soc.* **2015**, *450*, 905–925. [\[CrossRef\]](#)

86. Petrushevska, T.; Amanullah, R.; Goobar, A.; Fabbro, S.; Johansson, J.; Kjellsson, T.; Lidman, C.; Paech, K.; Richard, J.; Dahle, H.; et al. High-redshift supernova rates measured with the gravitational telescope A1689. *Astron. Astrophys.* **2016**, *594*, A54. [\[CrossRef\]](#)

87. Frohmaier, C.; Angus, C.R.; Vincenzi, M.; Sullivan, M.; Smith, M.; Nugent, P.E.; Cenko, S.B.; Gal-Yam, A.; Kulkarni, S.R.; Law, N.M.; et al. From core collapse to superluminous: The rates of massive stellar explosions from the Palomar Transient Factory. *Mon. Not. R. Astron. Soc.* **2020**, *500*, 5142–5158. [\[CrossRef\]](#)

88. Kobayashi, C.; Tsujimoto, T.; Nomoto, K. The History of the Cosmic Supernova Rate Derived from the Evolution of the Host Galaxies. *Astrophys. J.* **2000**, *539*, 26–38. [\[CrossRef\]](#)

89. Strolger, L.; Riess, A.G.; Dahlen, T.; Livio, M.; Panagia, N.; Challis, P.; Tonry, J.L.; Filippenko, A.V.; Chornock, R.; Ferguson, H.; et al. The Hubble Higher z Supernova Search: Supernovae to $z=1.6$ and Constraints on Type Ia Progenitor Models. *Astrophys. J.* **2004**, *613*, 200–223. [\[CrossRef\]](#)

90. Dahlen, T.; Strolger, L.; Riess, A.G.; Mobasher, B.; Chary, R.; Conselice, C.J.; Ferguson, H.C.; Fruchter, A.S.; Giavalisco, M.; Livio, M.; et al. High-Redshift Supernova Rates. *Astrophys. J.* **2004**, *613*, 189–199. [\[CrossRef\]](#)

91. Valiante, R.; Matteucci, F.; Recchi, S.; Calura, F. Theoretical cosmic Type Ia supernova rates. *New Astron.* **2009**, *14*, 638–648. [\[CrossRef\]](#)

92. Petrecca, V.; Botticella, M.T.; Cappellaro, E.; Greggio, L.; Sánchez, B.; Möller, A.; Sako, M.; Graham, M.; Paolillo, M.; Bianco, F.; et al. Recovered SN Ia rate from simulated LSST images. *arXiv* **2024**, arXiv:2402.17612.

93. Palicio, P.A.; Matteucci, F.; Valle, M.D.; Spitoni, E. Cosmic Type Ia SN rate and constraints on SN Ia progenitors. *arXiv* **2024**, arXiv:2402.16635.

94. Kobayashi, C.; Tsujimoto, T.; Nomoto, K.; Hachisu, I.; Kato, M. Metallicity effects on type Ia supernovae and cosmic supernova rates in cluster vs. field galaxies. *Mem. Soc. Astron. Ital.* **2000**, *71*, 461–470.

95. Toonen, S.; Nelemans, G.; Portegies Zwart, S. Supernova Type Ia progenitors from merging double white dwarfs: Using a new population synthesis model. *Astron. Astrophys.* **2012**, *546*, A70. [\[CrossRef\]](#)

96. Kistler, M.D.; Stanek, K.Z.; Kochanek, C.S.; Prieto, J.L.; Thompson, T.A. The Impact of Metallicity on the Rate of Type Ia Supernovae. *Astrophys. J.* **2013**, *770*, 88. [\[CrossRef\]](#)

97. Claeys, J.S.W.; Pols, O.R.; Izzard, R.G.; Vink, J.; Verbunt, F.W.M. Theoretical uncertainties of the Type Ia supernova rate. *Astron. Astrophys.* **2014**, *563*, A83. [\[CrossRef\]](#)

98. Maoz, D.; Mannucci, F. Type-Ia Supernova Rates and the Progenitor Problem: A Review. *Publ. Astron. Soc. Aust.* **2012**, *29*, 447–465. [\[CrossRef\]](#)

99. Pain, R.; Hook, I.; Perlmutter, S.; Deustua, S.; Gabi, S.; Goldhaber, G.; Groom, D.; Kim, A.; Kim, M.; Lee, J.; et al. The Type Ia Supernova Rate at $z \sim 0.4$. *arXiv* **1996**, arXiv:astro-ph/9602125.

100. Hardin, D.; Afonso, C.; Alard, C.; Albert, J.N.; Amadon, A.; Andersen, J.; Ansari, R.; Aubourg, E.; Bareyre, P.; Bauer, F.; et al. Type Ia supernova rate at $z \sim 0.1$. *arXiv* **2000**, arXiv:astro-ph/0006424.

101. Pain, R.; Fabbro, S.; Sullivan, M.; Ellis, R.S.; Aldering, G.; Astier, P.; Deustua, S.E.; Fruchter, A.S.; Goldhaber, G.; Goobar, A.; et al. The Distant Type Ia Supernova Rate. *Astrophys. J.* **2002**, *577*, 120–132. [\[CrossRef\]](#)

102. Madgwick, D.S.; Hewett, P.C.; Mortlock, D.J.; Wang, L. Spectroscopic Detection of Type Ia Supernovae in the Sloan Digital Sky Survey. *Astrophys. J.* **2003**, *599*, L33–L36. [\[CrossRef\]](#)

103. Tonry, J.L.; Schmidt, B.P.; Barris, B.; Candia, P.; Challis, P.; Clocchiatti, A.; Coil, A.L.; Filippenko, A.V.; Garnavich, P.; Hogan, C.; et al. Cosmological Results from High- z Supernovae. *Astrophys. J.* **2003**, *594*, 1–24. [\[CrossRef\]](#)

104. Blanc, G.; Afonso, C.; Alard, C.; Albert, J.N.; Aldering, G.; Amadon, A.; Andersen, J.; Ansari, R.; Aubourg, E.; Balland, C.; et al. Type Ia supernova rate at a redshift of ~ 0.1 . *Astron. Astrophys.* **2004**, *423*, 881–894. [\[CrossRef\]](#)

105. Scannapieco, E.; Bildsten, L. The Type Ia Supernova Rate. *Astrophys. J.* **2005**, *629*, L85–L88. [\[CrossRef\]](#)

106. Barris, B.J.; Tonry, J.L. The Rate of Type Ia Supernovae at High Redshift. *Astrophys. J.* **2006**, *637*, 427–438. [\[CrossRef\]](#)

107. Neill, J.D.; Sullivan, M.; Balam, D.; Pritchett, C.J.; Howell, D.A.; Perrett, K.; Astier, P.; Aubourg, E.; Basa, S.; Carlberg, R.G.; et al. The Type Ia Supernova rate at $z=0.5$ from the Supernova Legacy Survey. *Astron. J.* **2006**, *132*, 1126–1145. [\[CrossRef\]](#)

108. Neill, J.D.; Sullivan, M.; Balam, D.; Pritchett, C.J.; Howell, D.A.; Perrett, K.; Astier, P.; Aubourg, E.; Basa, S.; Carlberg, R.G.; et al. The Supernova Type Ia Rate Evolution with SNLS. *AIP Conf. Proc.* **2007**, *924*, 421–424. [\[CrossRef\]](#)

109. Poznanski, D.; Maoz, D.; Yasuda, N.; Foley, R.J.; Doi, M.; Filippenko, A.V.; Fukugita, M.; Gal-Yam, A.; Jannuzzi, B.T.; Morokuma, T.; et al. Supernovae in the Subaru Deep Field: An initial sample and Type Ia rate out to redshift 1.6. *Mon. Not. R. Astron. Soc.* **2007**, *382*, 1169–1186. [\[CrossRef\]](#)

110. Dahlen, T.; Strolger, L.; Riess, A.G. The Extended HST Supernova Survey: The Rate of SNe Ia at $z > 1.4$ Remains Low. *Astrophys. J.* **2008**, *681*, 462–469. [\[CrossRef\]](#)

111. Kuznetsova, N.; Barbary, K.; Connolly, B.; Kim, A.G.; Pain, R.; Roe, N.A.; Aldering, G.; Amanullah, R.; Dawson, K.; Doi, M.; et al. A New Determination of the High-Redshift Type Ia Supernova Rates with the Hubble Space Telescope Advanced Camera for Surveys. *Astrophys. J.* **2008**, *673*, 981–998. [\[CrossRef\]](#)

112. Dilday, B.; Kessler, R.; Frieman, J.A.; Holtzman, J.; Marriner, J.; Miknaitis, G.; Nichol, R.C.; Romani, R.; Sako, M.; Bassett, B.; et al. A Measurement of the Rate of Type Ia Supernovae at Redshift $z=0.1$ from the First Season of the SDSS-II Supernova Survey. *Astrophys. J.* **2008**, *682*, 262–282. [\[CrossRef\]](#)

113. Horesh, A.; Poznanski, D.; Ofek, E.O.; Maoz, D. The rate of Type Ia supernovae at $z=0.2$ from SDSS-I overlapping fields: Supernova rate from SDSS-I. *Mon. Not. R. Astron. Soc.* **2008**, *389*, 1871–1880. [\[CrossRef\]](#)

114. Graham, M.L.; Pritchett, C.J.; Sullivan, M.; Howell, D.A.; Gwyn, S.D.J.; Astier, P.; Balland, C.; Basa, S.; Carlberg, R.G.; Conley, A.; et al. The Type Ia Supernova Rate in Radio and Infrared Galaxies from the Canada-France-Hawaii Telescope Supernova Legacy Survey. *Astron. J.* **2010**, *139*, 594–605. [\[CrossRef\]](#)

115. Dilday, B.; Smith, M.; Bassett, B.; Becker, A.; Bender, R.; Castander, F.; Cinabro, D.; Filippenko, A.V.; Frieman, J.A.; Galbany, L.; et al. Measurements of the Rate of Type Ia Supernovae at Redshift <0.3 From the Sloan Digital Sky Survey II Supernova Survey. *Astrophys. J.* **2010**, *713*, 1026–1036. [\[CrossRef\]](#)

116. Dilday, B.; Bassett, B.; Becker, A.; Bender, R.; Castander, F.; Cinabro, D.; Frieman, J.A.; Galbany, L.; Garnavich, P.; Goobar, A.; et al. A Measurement of the Rate of Type Ia Supernovae in Galaxy Clusters from the SDSS-II Supernova Survey. *Astrophys. J.* **2010**, *715*, 1021–1035. [\[CrossRef\]](#)

117. Rodney, S.A.; Tonry, J.L. Revised Supernova Rates from the IfA Deep Survey. *Astrophys. J.* **2010**, *723*, 47–53. [\[CrossRef\]](#)

118. Barbary, K.; Aldering, G.; Amanullah, R.; Brodwin, M.; Connolly, N.; Dawson, K.S.; Doi, M.; Eisenhardt, P.; Faccioli, L.; Fadeyev, V.; et al. The Hubble Space Telescope Cluster Supernova Survey. II. The Type Ia Supernova Rate in High-Redshift Galaxy Clusters. *Astrophys. J.* **2011**, *745*, 32. [\[CrossRef\]](#)

119. Barbary, K.; Aldering, G.; Amanullah, R.; Brodwin, M.; Connolly, N.; Dawson, K.S.; Doi, M.; Eisenhardt, P.; Faccioli, L.; Fadeyev, V.; et al. The Hubble Space Telescope Cluster Supernova Survey. VI. The Volumetric Type Ia Supernova Rate. *Astrophys. J.* **2011**, *745*, 31. [\[CrossRef\]](#)

120. Krughoff, K.S.; Connolly, A.J.; Frieman, J.; SubbaRao, M.; Kilper, G.; Schneider, D.P. Spectroscopic Determination of the Low-Redshift Type Ia Supernova Rate from the SLOAN Digital Sky Survey. *Astrophys. J.* **2011**, *731*, 42. [\[CrossRef\]](#)

121. Sand, D.J.; Graham, M.L.; Bildfell, C.; Zaritsky, D.; Pritchett, C.; Hoekstra, H.; Just, D.W.; Herbert-Fort, S.; Sivanandam, S.; Foley, R.J.; et al. The Multi-Epoch Nearby Cluster Survey: Type Ia Supernova Rate Measurement in $z=0.1$ Clusters and the Late-Time Delay Time Distribution. *Astrophys. J.* **2012**, *746*, 163. [\[CrossRef\]](#)

122. Perrett, K.; Sullivan, M.; Conley, A.; González-Gaitán, S.; Carlberg, R.; Fouchez, D.; Ripoche, P.; Neill, J.D.; Astier, P.; Balam, D.; et al. Evolution in the Volumetric Type Ia Supernova Rate from the Supernova Legacy Survey. *Astron. J.* **2012**, *144*, 59. [\[CrossRef\]](#)

123. Graur, O.; Maoz, D. Discovery of 90 Type Ia supernovae among 700 000 Sloan spectra: The Type Ia supernova rate versus galaxy mass and star formation rate at redshift = 0.1. *Mon. Not. R. Astron. Soc.* **2013**, *430*, 1746–1763. [\[CrossRef\]](#)

124. Graur, O.; Rodney, S.A.; Maoz, D.; Riess, A.G.; Jha, S.W.; Postman, M.; Dahlen, T.; Holoi, T.W.S.; McCully, C.; Patel, B.; et al. Type-Ia Supernova Rates to Redshift 2.4 from CLASH: The Cluster Lensing and Supernova Survey with Hubble. *Astrophys. J.* **2014**, *783*, 28. [\[CrossRef\]](#)

125. Okumura, J.E.; Ihara, Y.; Doi, M.; Morokuma, T.; Pain, R.; Totani, T.; Barbary, K.; Takanashi, N.; Yasuda, N.; Aldering, G.; et al. The Type Ia supernovae rate with Subaru/XMM-Newton Deep Survey. *Publ. Astron. Soc. Jpn.* **2014**, *66*. [\[CrossRef\]](#)

126. Rodney, S.A.; Riess, A.G.; Strolger, L.G.; Dahlen, T.; Graur, O.; Casertano, S.; Dickinson, M.E.; Ferguson, H.C.; Garnavich, P.; Hayden, B.; et al. Type Ia Supernova Rate Measurements to Redshift 2.5 From CANDELS: Searching for Prompt Explosions in the Early Universe. *Astron. J.* **2014**, *148*, 13. [\[CrossRef\]](#)

127. Frohmaier, C.; Sullivan, M.; Nugent, P.E.; Smith, M.; Dimitriadis, G.; Bloom, J.S.; Cenko, S.B.; Kasliwal, M.M.; Kulkarni, S.R.; Maguire, K.; et al. The volumetric rate of normal type Ia supernovae in the local Universe discovered by the Palomar Transient Factory. *Mon. Not. R. Astron. Soc.* **2019**, *486*, 2308–2320. [\[CrossRef\]](#)

128. Perley, D.A.; Fremling, C.; Sollerman, J.; Miller, A.A.; Dahiwale, A.S.; Sharma, Y.; Bellm, E.C.; Biswas, R.; Brink, T.G.; Bruch, R.J.; et al. The Zwicky Transient Facility Bright Transient Survey. II. A Public Statistical Sample for Exploring Supernova Demographics. *Astrophys. J.* **2020**, *904*, 35. [\[CrossRef\]](#)

129. Sharon, A.; Kushnir, D. The ZTF-BTS Type Ia supernovae luminosity function is consistent with a single progenitor channel for the explosions. *Mon. Not. R. Astron. Soc.* **2021**, *509*, 5275–5297. [\[CrossRef\]](#)

130. Desai, D.D.; Kochanek, C.S.; Shappee, B.J.; Jayasinghe, T.; Stanek, K.Z.; Holoi, T.W.S.; Thompson, T.A.; Ashall, C.; Beacom, J.F.; Do, A.; et al. Supernova Rates and Luminosity Functions from ASAS-SN I: 2014–2017 Type Ia SNe and Their Sub-Types. *arXiv* **2023**, arXiv:2306.11100. [\[CrossRef\]](#)

131. MacFadyen, A.I.; Woosley, S.E. Collapsars: Gamma-Ray Bursts and Explosions in “Failed Supernovae”. *Astrophys. J.* **1999**, *524*, 262. [\[CrossRef\]](#)

132. Hirschi, R.; Meynet, G.; Maeder, A. Stellar evolution with rotation: XIII. Predicted GRB rates at various Z . *Astron. Astrophys.* **2005**, *443*, 581–591. [\[CrossRef\]](#)

133. Yoon, S.-C.; Langer, N. Evolution of rapidly rotating metal-poor massive stars towards gamma-ray bursts. *Astron. Astrophys.* **2005**, *443*, 643–648. [\[CrossRef\]](#)

134. Woosley, S.E.; Heger, A. The Progenitor Stars of Gamma-Ray Bursts. *Astrophys. J.* **2006**, *637*, 914–921. [\[CrossRef\]](#)

135. Yoon, S.C.; Langer, N.; Norman, C. Single star progenitors of long gamma-ray bursts: I. Model grids and redshift dependent GRB rate. *Astron. Astrophys.* **2006**, *460*, 199–208. [\[CrossRef\]](#)

136. Curti, M.; Mannucci, F.; Cresci, G.; Maiolino, R. The mass–metallicity and the fundamental metallicity relation revisited on a fully -based abundance scale for galaxies. *Mon. Not. R. Astron. Soc.* **2019**, *491*, 944–964. [\[CrossRef\]](#)

137. Curti, M.; Maiolino, R.; Curtis-Lake, E.; Chevallard, J.; Carniani, S.; D’Eugenio, F.; Looser, T.J.; Scholtz, J.; Charlot, S.; Cameron, A.; et al. JADES: Insights on the low-mass end of the mass–metallicity–star-formation rate relation at $3 < z < 10$ from deep JWST/NIRSpec spectroscopy. *arXiv* **2023**, arXiv:2304.08516.

138. Boco, L.; Lapi, A.; Chruslinska, M.; Donevski, D.; Sicilia, A.; Danese, L. Evolution of Galaxy Star Formation and Metallicity: Impact on Double Compact Object Mergers. *Astrophys. J.* **2021**, *907*, 110. [\[CrossRef\]](#)

139. Popesso, P.; Concas, A.; Cresci, G.; Belli, S.; Rodighiero, G.; Inami, H.; Dickinson, M.; Ilbert, O.; Pannella, M.; Elbaz, D. The main sequence of star-forming galaxies across cosmic times. *Mon. Not. R. Astron. Soc.* **2022**, *519*, 1526–1544. [\[CrossRef\]](#)

140. Chruścińska, M.; Nelemans, G.; Boco, L.; Lapi, A. The impact of the FMR and starburst galaxies on the (low metallicity) cosmic star formation history. *Mon. Not. R. Astron. Soc.* **2021**, *508*, 4994–5027. [\[CrossRef\]](#)

141. Chrimes, A.A.; Stanway, E.R.; Eldridge, J.J. Binary population synthesis models for core-collapse gamma-ray burst progenitors. *Mon. Not. R. Astron. Soc.* **2019**, *491*, 3479–3495. [\[CrossRef\]](#)

142. Ghirlanda, G.; Salvaterra, R. The Cosmic History of Long Gamma Ray Bursts. *arXiv* **2022**, arXiv:2206.06390. [\[CrossRef\]](#)

143. Gabrielli, F.; Lapi, A.; Boco, L.; Ugolini, C.; Costa, G.; Sgalletta, C.; Shepherd, K.; Di Carlo, U.N.; Bressan, A.; Limongi, M.; et al. The Cosmic Rate of Pair-Instability Supernovae. *arXiv* **2024**, arXiv:2408.13076. [\[CrossRef\]](#)

144. Davé, R. The galaxy stellar mass–star formation rate relation: Evidence for an evolving stellar initial mass function? *Mon. Not. R. Astron. Soc.* **2008**, *385*, 147–160. [\[CrossRef\]](#)

145. Fryer, C.L.; Lien, A.Y.; Fruchter, A.; Ghirlanda, G.; Hartmann, D.; Salvaterra, R.; Upton Sanderbeck, P.R.; Johnson, J.L. Properties of High-redshift Gamma-Ray Bursts. *Astrophys. J.* **2022**, *929*, 111. [\[CrossRef\]](#)

146. Lapi, A.; Gandolfi, G.; Boco, L.; Gabrielli, F.; Massardi, M.; Haridasu, B.S.; Baccigalupi, C.; Bressan, A.; Danese, L. Constraining the Initial Mass Function in the Epoch of Reionization from Astrophysical and Cosmological Data. *Universe* **2024**, *10*, 141. [\[CrossRef\]](#)

147. Mitra, S.; Chatterjee, A. Non-parametric reconstruction of photon escape fraction from reionization. *Mon. Not. R. Astron. Soc. Lett.* **2023**, *523*, L35–L39. [\[CrossRef\]](#)

148. Horiuchi, S.; Beacom, J.F. Revealing Type Ia Supernova Physics with Cosmic Rates and Nuclear Gamma Rays. *Astrophys. J.* **2010**, *723*, 329–341. [\[CrossRef\]](#)

149. Sana, H.; de Mink, S.E.; de Koter, A.; Langer, N.; Evans, C.J.; Gieles, M.; Gosset, E.; Izzard, R.G.; Bouquin, J.B.L.; Schneider, F.R.N. Binary Interaction Dominates the Evolution of Massive Stars. *Science* **2012**, *337*, 444–446. [\[CrossRef\]](#)

150. Moe, M.; Di Stefano, R. Mind Your Ps and Qs: The Interrelation between Period (P) and Mass-ratio (Q) Distributions of Binary Stars. *Astrophys. J. Suppl. Ser.* **2017**, *230*, 15. [\[CrossRef\]](#)

151. Winters, J.G.; Henry, T.J.; Jao, W.C.; Subasavage, J.P.; Chatelain, J.P.; Slatten, K.; Riedel, A.R.; Silverstein, M.L.; Payne, M.J. The Solar Neighborhood. XLV. The Stellar Multiplicity Rate of M Dwarfs Within 25 pc. *Astron. J.* **2019**, *157*, 216. [\[CrossRef\]](#)

152. Refregier, A.; Amara, A.; Kitching, T.D.; Rassat, A.; Scaramella, R.; Weller, J. Euclid Imaging Consortium Science Book. *arXiv* **2010**, arXiv:1001.0061.

153. Laureijs, R.; Amiaux, J.; Arduini, S.; Auguères, J.L.; Brinchmann, J.; Cole, R.; Cropper, M.; Dabin, C.; Duvet, L.; Ealet, A.; et al. Euclid Definition Study Report. *arXiv* **2011**, arXiv:1110.3193.

154. Feindt, U.; Nordin, J.; Rigault, M.; Brinnel, V.; Dhawan, S.; Goobar, A.; Kowalski, M. *simsurvey*: Estimating transient discovery rates for the Zwicky transient facility. *J. Cosmol. Astropart. Phys.* **2019**, *2019*, 005.

155. Regős, E.; Vinkó, J. Detection and Classification of Supernovae Beyond $z \sim 2$ Redshift with the James Webb Space Telescope. *Astrophys. J.* **2019**, *874*, 158. [\[CrossRef\]](#)

156. Rose, B.M.; Baltay, C.; Hounsell, R.; Macias, P.; Rubin, D.; Scolnic, D.; Aldering, G.; Bohlin, R.; Dai, M.; Deustua, S.E.; et al. A Reference Survey for Supernova Cosmology with the Nancy Grace Roman Space Telescope. *arXiv* **2021**, arXiv:2111.03081.

157. Kocevski, D.; West, A.A.; Modjaz, M. Modeling the GRB Host Galaxy Mass Distribution: Are GRBs Unbiased Tracers of Star Formation? *Astrophys. J.* **2009**, *702*, 377. [\[CrossRef\]](#)

158. Vergani, S.D.; Salvaterra, R.; Japelj, J.; Le Floc'h, E.; D’Avanzo, P.; Fernandez-Soto, A.; Krühler, T.; Melandri, A.; Boissier, S.; Covino, S.; et al. Are long gamma-ray bursts biased tracers of star formation? Clues from the host galaxies of the Swift/BAT6 complete sample of LGRBs—I. Stellar mass at $z < 1$. *Astron. Astrophys.* **2015**, *581*, A102. [\[CrossRef\]](#)

159. Perley, D.A.; Tanvir, N.R.; Hjorth, J.; Laskar, T.; Berger, E.; Chary, R.; de Ugarte Postigo, A.; Fynbo, J.P.U.; Krühler, T.; Levan, A.J.; et al. The Swift GRB Host Galaxy Legacy Survey. II. Rest-Frame Near-IR Luminosity Distribution and Evidence for a Near-Solar Metallicity Threshold. *Astrophys. J.* **2016**, *817*, 8. [\[CrossRef\]](#)

160. Vergani, S.D.; Palmerio, J.; Salvaterra, R.; Japelj, J.; Mannucci, F.; Perley, D.A.; D’Avanzo, P.; Krühler, T.; Puech, M.; Boissier, S.; et al. The chemical enrichment of long gamma-ray bursts nurseries up to $z = 2$. *Astron. Astrophys.* **2017**, *599*, A120. [\[CrossRef\]](#)

161. Palmerio, J.T.; Vergani, S.D.; Salvaterra, R.; Sanders, R.L.; Japelj, J.; Vidal-García, A.; D’Avanzo, P.; Corre, D.; Perley, D. A.; Shapley, A.E.; et al. Are long gamma-ray bursts biased tracers of star formation? Clues from the host galaxies of the Swift/BAT6 complete sample of bright LGRBs—III. Stellar masses, star formation rates, and metallicities at $z > 1$. *Astron. Astrophys.* **2019**, *623*, A26. [\[CrossRef\]](#)

162. Langer, N.; Norman, C.A. On the Collapsar Model of Long Gamma-Ray Bursts: Constraints from Cosmic Metallicity Evolution. *ApJL* **2006**, *638*, L63–L66. [[CrossRef](#)]

163. White, N.E.; Bauer, F.E.; Baumgartner, W.; Bautz, M.; Berger, E.; Cenko, B.; Chang, T.C.; Falcone, A.; Fausey, H.; Feldman, C.; et al. The Gamow Explorer: A Gamma-Ray Burst Observatory to study the high redshift universe and enable multi-messenger astrophysics. In *Proceedings of the UV, X-ray, and Gamma-Ray Space Instrumentation for Astronomy XXII*; Society of Photo-Optical Instrumentation Engineers (SPIE) Conference Series; Siegmund, O.H., Ed.; SPIE: St Bellingham, WA, USA, 2021; Volume 11821, p. 1182109. [[CrossRef](#)]

164. Bozzo, E.; Amati, L.; Baumgartner, W.; Chang, T.C.; Cordier, B.; Angelis, N.D.; Doi, A.; Feroci, M.; Froning, C.; Gaskin, J.; et al. Future Perspectives for Gamma-ray Burst Detection from Space. *arXiv* **2024**, arXiv:2404.11808. [[CrossRef](#)]

165. Foley, R.J.; Koekemoer, A.M.; Spergel, D.N.; Bianco, F.B.; Capak, P.; Dai, L.; Dore, O.; Fazio, G.G.; Ferguson, H.; Filippenko, A.V.; et al. LSST Observing Strategy White Paper: LSST Observations of WFIRST Deep Fields. *arXiv* **2018**, arXiv:1812.00514. [[CrossRef](#)]

166. Foley, R.; Bloom, J.S.; Cenko, S.B.; Chornock, R.; Dimitriadis, G.; Doré, O.; Filippenko, A.V.; Fox, O.D.; Hirata, C.M.; Jha, S.W.; et al. WFIRST: Enhancing Transient Science and Multi-Messenger Astronomy. *Bull. Am. Astron. Soc.* **2019**, *51*, 305. [[CrossRef](#)]

167. Moriya, T.J.; Wong, K.C.; Koyama, Y.; Tanaka, M.; Oguri, M.; Hilbert, S.; Nomoto, K. Searches for Population III pair-instability supernovae: Predictions for ULTIMATE-Subaru and WFIRST. *Publ. Astron. Soc. Jpn.* **2019**, *71*, 59. [[CrossRef](#)]

168. Wang, L.; Mould, J.; Baade, D.; Baron, E.; Bromm, V.; Cooke, J.; Fan, X.; Foley, R.; Fruchter, A.; Gal-Yam, A.; et al. JWST: Probing the Epoch of Reionization with a Wide Field Time-Domain Survey. *Bull. Am. Astron. Soc.* **2019**, *51*, 399. [[CrossRef](#)]

169. Dessart, L.; Prieto, J.L.; Hillier, D.J.; Kuncarayakti, H.; Hueichapan, E.D. Using LSST late-time photometry to constrain Type Ibc supernovae and their progenitors. *Astron. Astrophys.* **2022**, *666*, L14. [[CrossRef](#)]

170. Bailey, A.C.; Vincenzi, M.; Scolnic, D.; Cuillandre, J.C.; Rhodes, J.; Hook, I.; Peterson, E.R.; Popovic, B. Type Ia supernova observations combining data from the Euclid mission and the Vera C. Rubin Observatory. *Mon. Not. R. Astron. Soc.* **2023**, *524*, 5432–5441. [[CrossRef](#)]

171. Subrayan, B.M.; Milisavljevic, D.; Moriya, T.J.; Weil, K.E.; Lentner, G.; Linvill, M.; Banovetz, J.; Garretson, B.; Reynolds, J.; Sravan, N.; et al. Inferencing Progenitor and Explosion Properties of Evolving Core-collapse Supernovae from Zwicky Transient Facility Light Curves. *Astrophys. J.* **2023**, *945*, 46. [[CrossRef](#)]

172. Arendse, N.; Dhawan, S.; Carracedo, A.S.; Peiris, H.V.; Goobar, A.; Wojtak, R.; Alves, C.; Biswas, R.; Huber, S.; Birrer, S.; et al. Detecting strongly-lensed type Ia supernovae with LSST. *arXiv* **2024**, arXiv:2312.04621. [[CrossRef](#)]

173. Strotjohann, N.L.; Ofek, E.O.; Gal-Yam, A.; Sollerman, J.; Chen, P.; Yaron, O.; Zackay, B.; Rehmetulla, N.; Gris, P.; Masci, F.J.; et al. Search for Supernova Progenitor Stars with ZTF and LSST. *Astrophys. J.* **2023**, *960*, 72. [[CrossRef](#)]

174. Salvaterra, R.; Campana, S.; Vergani, S.D.; Covino, S.; D’Avanzo, P.; Fugazza, D.; Ghirlanda, G.; Ghisellini, G.; Melandri, A.; Nava, L.; et al. A Complete Sample of Bright Swift Long Gamma-Ray Bursts. I. Sample Presentation, Luminosity Function and Evolution. *Astrophys. J.* **2012**, *749*, 68. [[CrossRef](#)]

Disclaimer/Publisher’s Note: The statements, opinions and data contained in all publications are solely those of the individual author(s) and contributor(s) and not of MDPI and/or the editor(s). MDPI and/or the editor(s) disclaim responsibility for any injury to people or property resulting from any ideas, methods, instructions or products referred to in the content.